REPORT DOCUMENTATION PAGE

Form Approved
OMB No. 0704-0188

1. REPORT DATE (*DD-MM-YYYY*)	2. REPORT TYPE	3. DATES COVERED (*From - To*)
01-10-2010	Final Technical	01-06-2004 -- 30-11-2009

4. TITLE AND SUBTITLE
(U) (MURI04) Experimental/Computational Studies of Combined Cycle Propulsion: Physics and Transient Phenomena in Inlets and Scramjet Combustors

5a. CONTRACT NUMBER

5b. GRANT NUMBER
FA9550-04-1-0387

5c. PROGRAM ELEMENT NUMBER
61103F

6. AUTHOR(S)
N. Clemens (PI), M. Akella, M. Cappelli, D. Dolling, R. Hanson, S. Lele, M. Mungal, L. Raja

5d. PROJECT NUMBER
5094

5e. TASK NUMBER
RS

5f. WORK UNIT NUMBER

7. PERFORMING ORGANIZATION NAME(S) AND ADDRESS(ES)
The University of Texas at Austin
Aerospace Engineering Department
Austin TX 78712-1085

8. PERFORMING ORGANIZATION REPORT NUMBER

9. SPONSORING / MONITORING AGENCY NAME(S) AND ADDRESS(ES)
AFOSR/RSA
875 North Randolph Street
Suite 325, Room 3112
Arlington VA 22203-1768

10. SPONSOR/MONITOR'S ACRONYM(S)

11. SPONSOR/MONITOR'S REPORT NUMBER(S)
AFRL-OSR-VA-TR-2013-0901

12. DISTRIBUTION / AVAILABILITY STATEMENT
Approved for public release; distribution is unlimited

13. SUPPLEMENTARY NOTES

14. ABSTRACT
The major accomplishments of an AFOSR-MURI grant focused on transient processes in hypersonic combined-cycle propulsion are described. This effort had two main thrusts: investigation of (i) inlet-isolator physics and unstart control, and (ii) supersonic mixing, combustion and flameholding. The supported work led to new findings related to the physics of shock-induced turbulent separation and inlet unstart, closed loop control of inlet unstart, development of kilohertz repetition rate plasma actuators, understanding of non-equilibrium plasma enhancement of combustion in subsonic and supersonic flameholders, development of the large-eddy simulation technique for compressible jets-in-crossflow, and development of new tunable diode-laser diagnostics for supersonic combustors. The scientific results obtained from this MURI program were disseminated widely to the scientific community via archival journal publications and technical conferences. The MURI effort led to 28 submitted or published papers in archival journals and 8 Ph.D. dissertations.

15. SUBJECT TERMS
Propulsion, Hypersonic, Supersonic, Inlet, Combustion, Simulation, Diagnostics

16. SECURITY CLASSIFICATION OF:			17. LIMITATION OF ABSTRACT	18. NUMBER OF PAGES	19a. NAME OF RESPONSIBLE PERSON
a. REPORT	b. ABSTRACT	c. THIS PAGE			Julian M. Tishkoff
Unclassified	Unclassified	Unclassified	UL	54	19b. TELEPHONE NUMBER (*include area code*) (703)696-8478

20130919115

Experimental/Computational Studies of Combined-Cycle Propulsion: Physics and Transient Phenomena in Inlets and Scramjet Combustors

TABLE OF CONTENTS

1. SUMMARY OF ACTIVITIES

This report summarizes the activities and major findings of a MURI center dedicated to studies of transient processes relevant to combined cycle engines for hypersonic flight. The center was a collaborative effort between researchers at The University of Texas at Austin and Stanford University. The over-arching objectives of this research program were to investigate the physics and control of inlet-isolator unstart and to develop new understanding of supersonic combustion and flame-holding. Meeting these objectives required the development of novel plasma actuators and tunable diode laser diagnostics, as well as improved methods for conducting large-eddy simulations (LES) of compressible turbulent flows. The work focused on the following five tasks:

(i) **Experimental studies of unsteady and transient processes in inlet/isolators**. This topic focused on studies of (1) the unsteadiness of shock-induced turbulent separation in canonical compression ramp interactions and (2) unstart physics of a simplified inlet-isolator model. This work was conducted in the supersonic wind tunnel at UT-Austin.

(ii) **Closed-Loop Control of Unstart.** This work focused on the development of flow-control techniques to arrest unstart once it begins. The effort required the development of fast-acting fluidic actuators, new feedback-control algorithms and new unstart-detection schemes.

(iii) **Active and passive control of combustor flows.** This work was aimed at developing new strategies for achieving rapid ignition, stable flame-holding and efficient combustion in a simplified scramjet combustor. This work was conducted in the expansion tube facility at Stanford. A key aspect of this task was to development new diode laser-based sensors to aid in the control of scramjet combustors.

(iv) **Characterization and development of plasma-enhanced combustion and plasma-actuators for high-speed flow control.** A major effort was conducted to identify fundamental processes involved in combustion ignition and stabilization enhancements in high-speed flows by using pulsed (~10-100 ns), high-repetition rate (10-100 kHz) high intensity (1 – 10 kV) discharges. Additionally, new high-bandwidth plasma actuators were developed to enable the control of high-speed unsteady flows such as those that occur in aircraft inlets.

(v) **Development of a high-fidelity, LES code to conduct numerical simulations of transient processes in a scramjet engine**. High-fidelity large-eddy-simulations (LES) of a supersonic jet in a supersonic cross-flow were conducted. These simulations advanced the state-of-the-art of LES for high-speed compressible flows and revealed new physics of the complex turbulent mixing process.

2. PERSONNEL SUPPORTED WITH THIS EFFORT

a) Faculty (The University of Texas at Austin)

Dr. David S. Dolling – Professor (original Principal investigator)

Dr. Noel T. Clemens –Professor (Principal investigator)

Dr. Maruthi Akella – Associate Professor

Dr. Laxminarayan Raja – Associate Professor

b) Faculty (Stanford University)

Dr. Godfrey Mungal – Professor

Dr. Ronald Hanson – Professor

Dr. Sanjiva Lele – Professor

Dr. M Cappelli –Professor

c) Professional Researchers

Dr. Bulent Yuceil – Post Doctoral Fellow (UT Austin)

Dr. Jay B. Jeffries – Senior Research Scientist (Stanford University)

Dr. David F. Davidson – Senior Research Scientist (Stanford University)

Dr. Soshi Kawai – Post Doctoral Fellow (Stanford University)

Dr. Benoit Fiorina – Post Doctoral Fellow (Stanford University)

d) Graduate Students supported all or in part on this grant

Justin Wagner – Graduate Student (UT Austin)

Agustin Valdivia – Graduate Student (UT Austin)

John Hatlelid – Graduate Student (UT Austin)

Sukumar Srikant – Graduate Student (UT Austin)

James Doyle – Graduate Student (UT Austin)

Venkat Narayanaswamy – Graduate Student (UT Austin)

Jichul Shin – Graduate Student (UT Austin)

Shankar Mahadevan – Graduate Student (UT Austin)

Thomas Deconinck - Graduate Student (UT Austin)

John Hatlelid – Graduate Student (UT Austin)

Andree J. Houle– Graduate Student (Stanford University)

Will Heltsey – Graduate Research Assistant (Stanford University)

Chris Strand – Graduate Research Assistant (Stanford University)

Hyungrok Do – Graduate Research Assistant (Stanford University)

Wookyung Kim – Graduate Research Assistant (Stanford University)

3. ACCOMPLISHMENTS / NEW FINDINGS

The major accomplishment and findings of this joint research program are detailed below. This report gives only a brief summary of the extensive research that was conducted over the 5-year term of the grant. For more detailed information, the reader can consult the extensive number of journal papers (Sec. 5) or Ph.D. dissertations (Sec. 6) that were published under sponsorship of this grant.

3.1 Physics of Shock-Induced Turbulent Separation (PIs: Clemens, Dolling)

Inlets and isolators are dominated by shock wave/boundary layer interactions that are separated and exhibit extreme unsteadiness [1]. The separated flow and its unsteadiness play important roles in inlet-isolator unstart because they lead to flow blockage and instability; therefore, a major objective of our work was to improve our knowledge of the mechanisms that drive the low-frequency unsteadiness of shock-induced turbulent separation. Such knowledge can be used to develop new physics-based control schemes to control inlet instability and unstart. The flow studied was a Mach 2 compression ramp interaction. The experiments were conducted in the High-Speed Wind Tunnel Laboratory at The University of Texas at Austin. The major accomplishments of this work are as follows:

1. For the first time, plan view particle image velocimetry (PIV) revealed the presence of very large scale coherent structures in the Mach 2 turbulent boundary layer
2. These superstructures were shown to be coherent over a length scale as large as 30 boundary layer thicknesses
3. Studies of a Mach 2 compression ramp interaction showed that the superstructures were correlated with large-scale pulsation of the separated flow.
4. Our analysis of these data and those of other researchers suggests a new view of unsteadiness of shock/boundary layer unsteadiness: for weak interactions, the unsteadiness is governed mainly by the upstream turbulent boundary layers, whereas for strong interactions, it is driven more by an entrainment instability intrinsic to the separation bubble.

3.1.1 Measurements of Unsteadiness of Mach 2 Compression Ramp Interactions

At the time that the research began, the underlying mechanisms that drive the low-frequency unsteadiness of shock-induced turbulent separation were not well understood [2]. Previous work was somewhat contradictory, as some studies showed that the unsteadiness was driven by the upstream fluctuations, whereas others showed that it was driven by a downstream mechanism. We have focused heavily on an exploration of the potential impact of fluctuations in the upstream turbulent boundary layer.

To enable the investigation of the interaction dynamics, high-speed PIV, at a rate of 6 kHz, was conducted in streamwise-spanwise planes. The 6 kHz PIV framing rate was sufficient to resolve the low-frequency motion of the separated flow. It also was found that the structure of the upstream boundary layer could be visualized effectively by placing sequential images of the movie side-by-side in accordance with Taylor's frozen flow hypothesis. The magnitude of the displacement between consecutive images was determined by assuming that the flow convected at a velocity of $0.9U_\infty$ during the interframe period of 167 μs. This same technique was used previously with planar laser Mie scattering time sequences. Two sample composite images, composed of 10 movie frames each, are shown in Fig. 1. These images give an approximate indication of the instantaneous boundary layer structure over a region that extends to a distance of 40δ upstream of the compression ramp, where δ is the 99% velocity boundary layer thickness. What is seen is quite remarkable since the long strips of uniform momentum fluid (i.e., superstructures [3]) seem to extend to as much as 30δ in the streamwise direction. The importance of this observation is that there exist structures in the boundary layer that are large enough to account for the low-frequency motions (< a few kHz) of the separated flow.

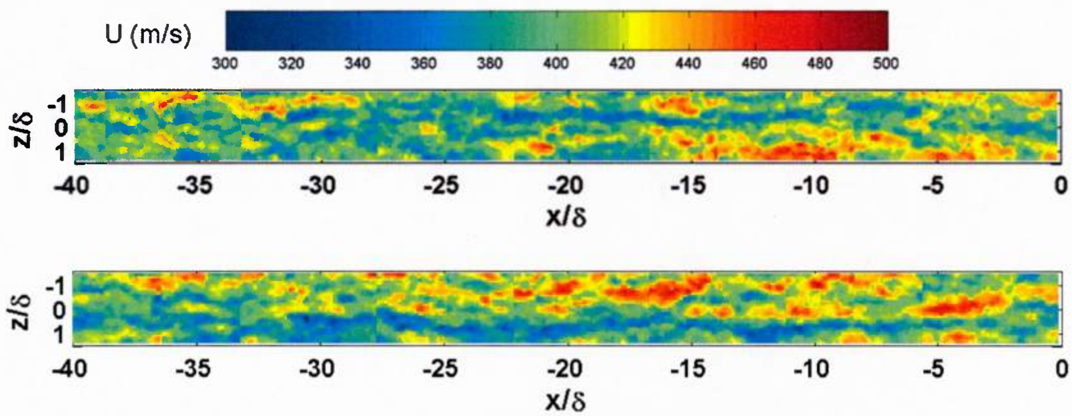

Figure 1. Plan-view velocity fields in the boundary layer upstream of a Mach 2 compression ramp interaction. The ramp corner is at x/δ =0. Two sample images are shown. Each image represents a composite of 10 consecutive frames taken from a 6 kHz movie sequence and placed "side-by-side" in accordance with Taylor's frozen flow hypothesis. The sheet location is y/δ=0.2.

To investigate the time correlation between the upstream boundary layer velocity fluctuations and the separated flow motion, a surrogate for the instantaneous separation line was used. For this analysis, a Cartesian coordinate system is used, where x, y and z designate the streamwise, wall normal and cross stream coordinates, respectively. A surrogate for the separation line was necessary because at y/δ=0.2, the actual location where the shear stress goes to zero could not be determined. The surrogate was defined arbitrarily as the location where the velocity was $U = \overline{U} - 4\sigma$ (with $\overline{U}$ the mean velocity and σ the standard deviation). This assumption was checked with previously acquired side view PIV data in the same flow, which showed that the surrogate is consistently downstream of the true separation point but is correlated highly with it. An example image with the separation line surrogate rendered as a white dotted line is shown in Fig. 2. Also shown is a red line that extends into the upstream boundary layer. The velocity was averaged along this red line to give the line-averaged velocity U_l. Fig. 3a shows the time series of U_l/δ that has been low-pass filtered to 1 kHz, and Fig. 3b shows the time series of the separation surrogate location. These two waveforms are very similar, which indicates a strong correlation between the upstream boundary layer fluctuations and motion of the separation line. The cross correlation of these filtered data gives a correlation coefficient of 0.85, which indicates there is nearly a one-to-one correspondence between the two waveforms.

Figure 3 shows that the separated flow unsteadiness of this interaction is driven by velocity fluctuations in the upstream boundary layer. Furthermore, the correlation is stronger for the lower frequency fluctuations, and these low frequency fluctuations clearly are related to the large-scale coherent structures in the upstream boundary layer. The movies taken further show that the separated flow seems to respond to global changes in momentum in the upstream boundary layer. To investigate this potential relationship, for each PIV frame the velocity upstream of the separated flow was averaged, and the time series of this averaged velocity was correlated to the average separated flow scale. These time series are not shown here for brevity, but they do show a strong correlation, albeit not as strong as for the low-pass filtered data. For example, the resulting correlation coefficient was 0.7, as compared to the low-pass filtered value of 0.85; nevertheless, the strong correlation shows that the separated flow responds to global changes in the upstream boundary layer and not just to the large-scale coherent structures.

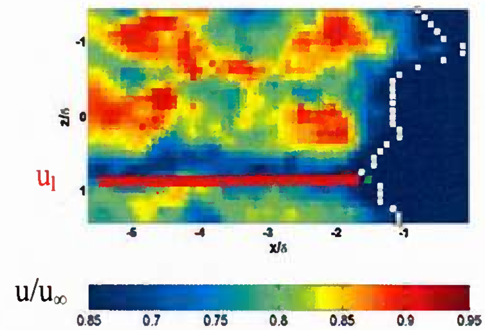

Figure 2. Plan-view wide-field PIV contour plots of the *U*-velocity in a Mach 2 compression ramp interaction. The images show the upstream boundary layer and the separated flow region (deep blue). The ramp corner is at x/δ =0. The white dotted line is the separation line surrogate. The green dot is the instantaneous separation point (x_{sep}) that was monitored in the analysis. The velocity was averaged along the red line to give the line-averaged velocity U_l.

These results are important because they suggest that methods that seek to control shock-induced separated flows may have the greatest effectiveness by perturbing the flow in the upstream boundary layer.

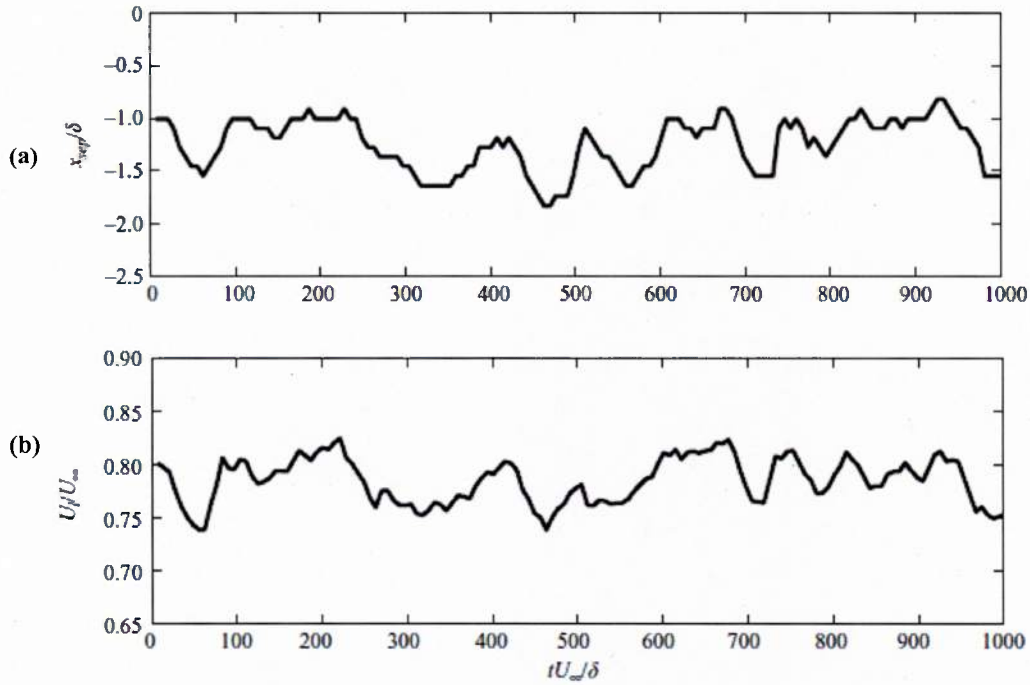

Figure 3. Sample time series of (a) $U_l(t)/U_\infty$ and (b) $x_{sep}(t)/\delta$, where both time-series were low-pass filtered to a frequency of 1 kHz. The correlation coefficient is 0.8.

3.2 Inlet Unstart Dynamics (PIs: Clemens, Dolling)

A major objective of this work was to improve knowledge of the flow inside hypersonic inlets and isolators. Toward this end a simplified inlet-isolator model was developed and tested in the Mach 5 wind tunnel at The University of Texas at Austin. The model could be unstarted by raising a flap downstream of the isolator, which simulated the pressure rise due to combustion. By adjusting the angle of the flap, the flow in a fully supersonic mode (scramjet) or subsonic mode (ramjet) could be studied. If the flap were raised sufficiently, then unstart would be initiated. Extensive PIV measurements were made of the scramjet, ramjet, and unstarted flows. The major accomplishments of this work are summarized as follows:

1. A new simplified hypersonic inlet-isolator wind tunnel model was developed. A downstream flap was used to change the back pressure and initiate unstart.
2. Extensive characterization of the flow was made with schlieren imaging, fast-response pressure measurements, and particle image velocimetry.
3. Extensive high-quality data were obtained that are ideal for validation of numerical simulations.

4. Measurements reveal that the unstart dynamics are influenced strongly by the degree of boundary layer separation in the inlet.
5. Three-dimensional effects are important during unstart since the boundary layers separate preferentially on the sidewalls at the beginning of unstart.

3.2.1 Unsteady Measurements of Inlet-Isolator Operation and Unstart

A schematic of the inlet/isolator model mounted to the floor of the Mach 5 wind tunnel is shown in Fig 4. The inlet is a six-degree half angle compression ramp, which is followed by a constant area isolator with an aspect ratio of 2. A 10-Hz PIV system was used to obtain velocity fields during unstart. The flow was imaged with three cameras to produce the wide field of view seen in Fig. 4 (shaded green). In addition, fast-response pressure measurements with 7 Kulite transducers were used to provide instantaneous wall pressure distributions. Unstart was induced by raising the flap near the isolator exit. Figure 5 shows the pressure time history of the most downstream transducer during a flap motion sequence. From 0 to 0.05 s, the flap is in the fully-down position, and the flow throughout the inlet/isolator is started and fully supersonic. At t = 0.05 s, the flap is raised gradually, which raises the T1 pressure until unstart occurs at t = 0.2 s, resulting in the labeled unstart event. An oscillatory unstarted flow (f = 124 Hz), which is seen more clearly in the figure inset, follows until t = 0.5 s. At this time the flap is lowered slightly, which results in a different unstarted flow that is non-oscillatory. At t = 1.0 s the flap is raised slightly, which results in another oscillatory unstarted flow with lower pressure fluctuations than the first oscillatory case. Finally, at t = 1.4 s, the flap is lowered, resulting in restart.

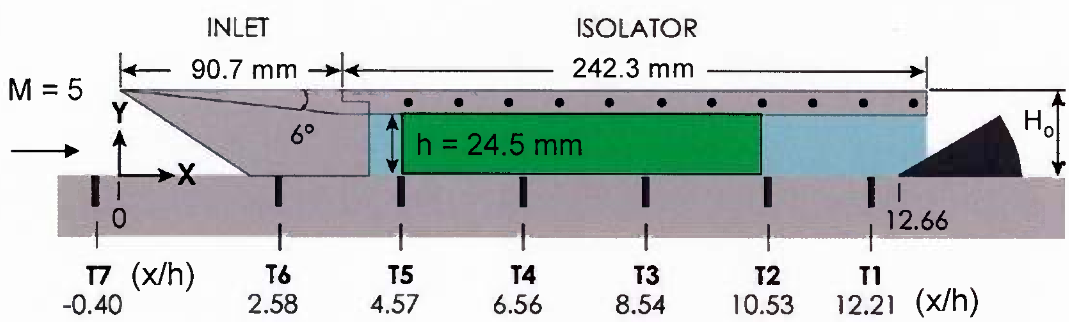

Figure 4. Schematic diagram of the inlet/isolator model mounted on the floor of the test section of the Mach 5 windtunnel.

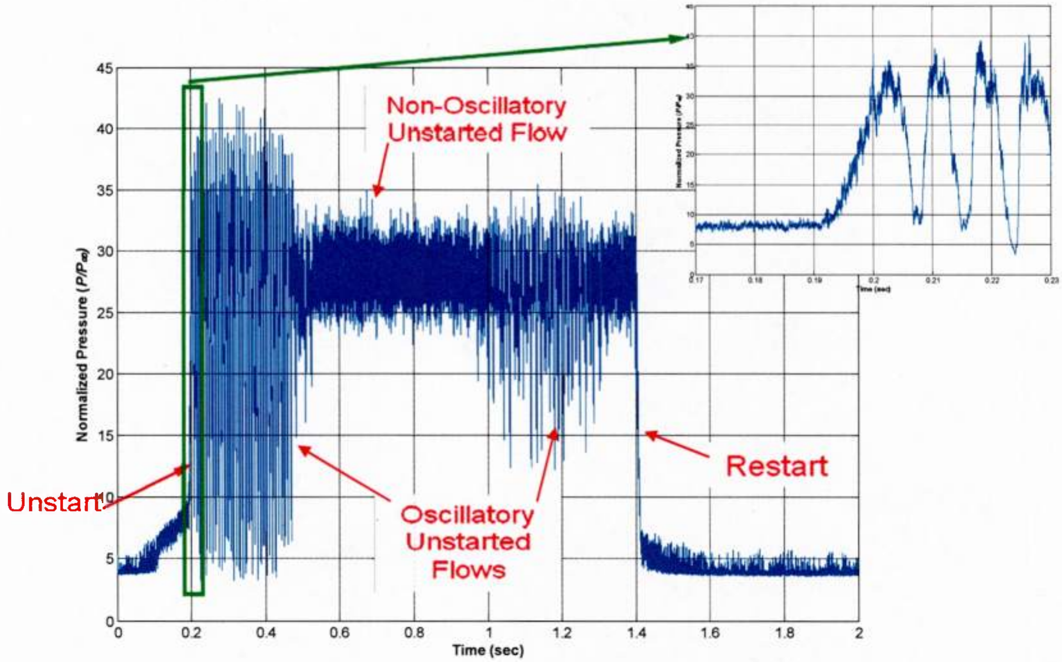

Figure 5. Most-downstream pressure transducer (T1) time history showing unstart, unstarted flows and restart.

In order to understand the flow structure of unstart, it is useful first to characterize the flowfield prior to unstart. Figure 6 shows the mean streamwise and wall-normal velocity contours, as well as an instantaneous Schlieren image (Fig. 6a) corresponding to the fully-supersonic flow. The Schlieren image shows the first three reflections of the compression ramp shock (arrows A, B and C). The streamwise velocity contours (Fig. 6b) clearly capture the thick floor boundary layer, and the wall-normal contours (Fig. 6c) are consistent with shock-expansion theory.

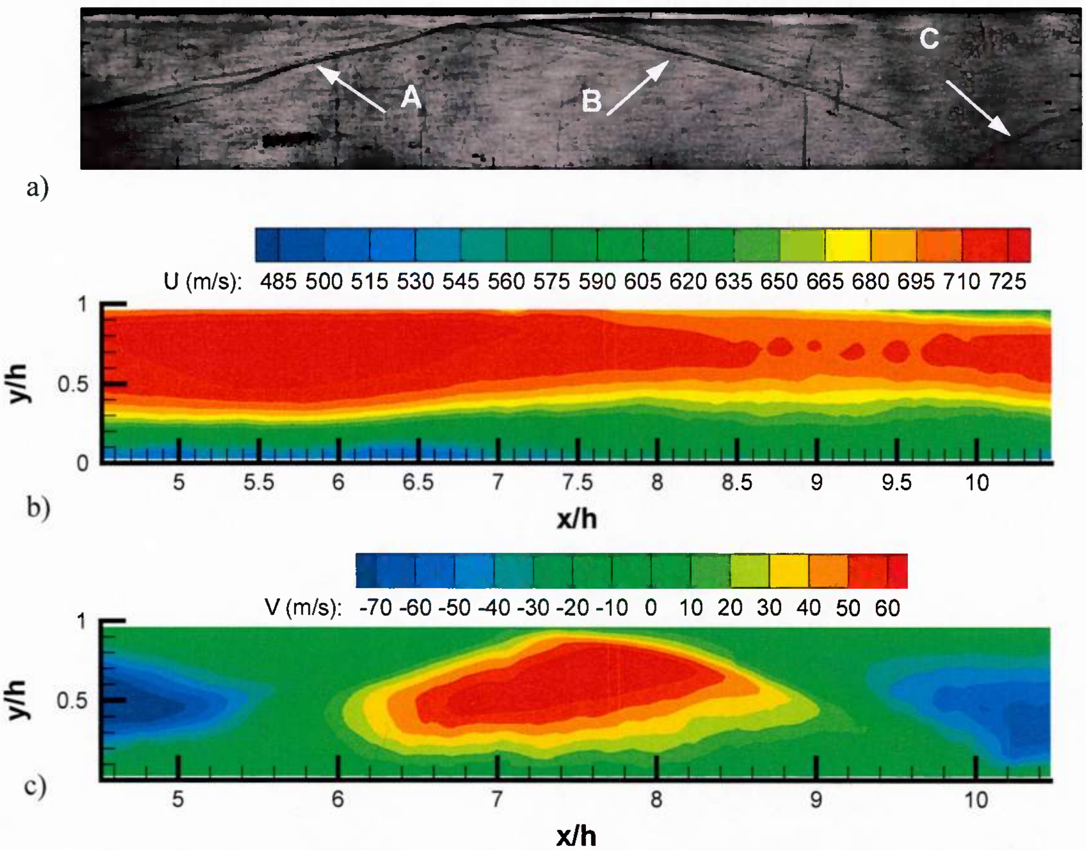

Figure 6. Fully-supersonic (started) flow. (a) Schlieren Image, (b) Mean streamwise velocity contours, and (c) Mean wall-normal velocity contours.

In order to understand how unstart propagates upstream through the inlet/isolator, a "pseudo-sequence" of PIV data was obtained beginning at the onset of unstart, which is defined to be $t = 0$ ms. The sequence includes data at times of $t = 2, 4, 5, 6, 7, 11$ and 14 ms during the unstart process; however, only the PIV data at $t = 6$ ms are presented in Fig. 7. In addition, a representative schlieren image is provided to give an indication of the flow structure. The Schlieren image shows that unstart has progressed upstream with the

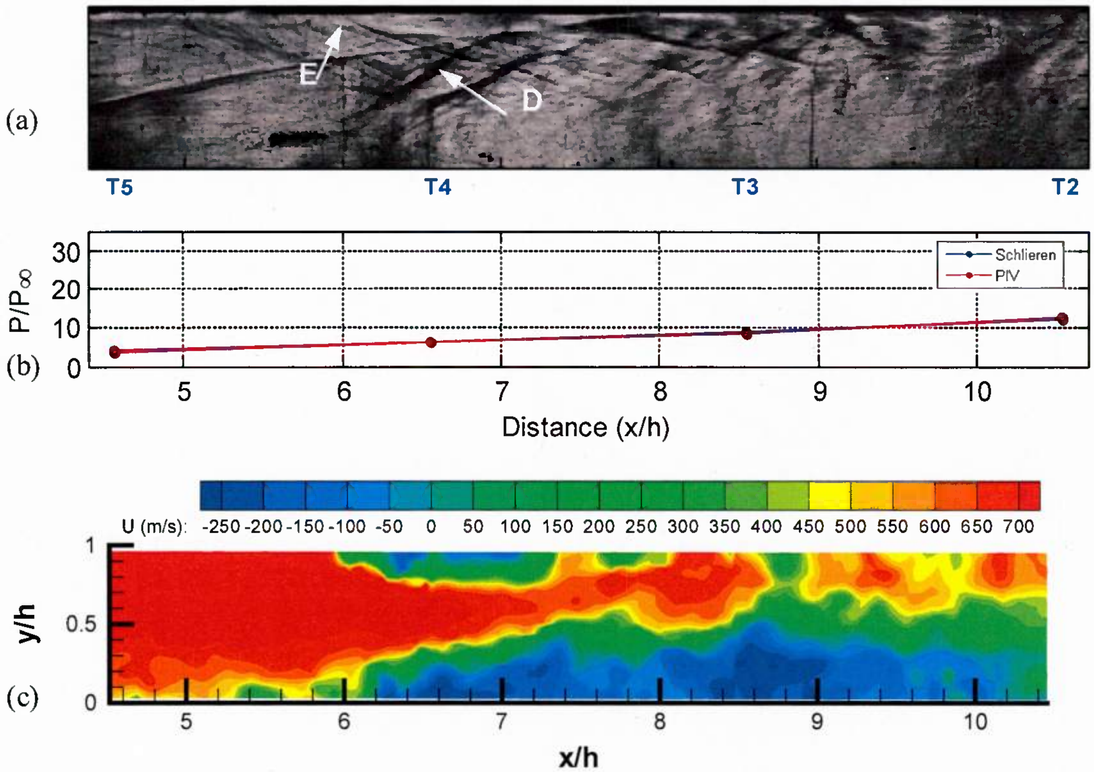

Figure 7. Unstart at t = 6ms. (a) Schlieren Image, (b) Wall Pressures corresponding to schlieren image and PIV data, and (c) Streamwise Velocity Contours.

formation of a strong shock system (arrow D) and the isolator ceiling boundary layer has separated (arrow E). These effects of unstart progression also are seen clearly in the PIV vector and streamwise velocity plots of Fig. 7c. In addition, the PIV data show intense separation of the floor boundary layer and regions of highly reversed flow with velocities reaching nearly -300 m/s. As unstart progresses upstream through the field of view, the flow first separates near the floor impingement location of the second reflected oblique shock. The strength of separation and amount of reverse flow increase as the unstart shock system moves further upstream. When the unstart shock system reaches a location near the ceiling impingement point of the first reflected oblique shock the ceiling boundary layer separates. These observations suggest that the initial oblique shock system in the inlet/isolator prior to unstart has an effect on the flow structure and dynamics of the unstart process.

3.3 Feedback Control of Inlet Unstart (PIs: Akella, Clemens)

The objective of this topic was to develop methods for obtaining feedback-control of inlet unstart. Achieving this objective involved an extensive series of experiments to identify a successful fast-acting pulsed actuator suitable for future control studies. In addition, it was necessary to identify unstart precursor signals that could be used in the closed-loop control algorithm. Finally, we wanted to develop a robust controller that effectively could stop unstart by using the actuator and unstart-precursor identified in the other parts of the study. The major accomplishments of this work are summarized as follows:

1. Open loop studies showed that unstart could be influenced by employing pulsed vortex-generator jets, combined with fixed ramp-type vortex generators, on the sidewalls of the inlet. These jets could be actuated on the order of 1 ms.
2. A simple threshold-based control scheme was applied to demonstrate that unstart could be arrested successfully about 50% of the time.
3. A more robust unstart detection method was developed that relies on elevated energy in a particular frequency band for the furthest downstream transducer.
4. New classes of low-order dynamic models were created of isentropic inlets with normal and oblique shocks. These models were validated with experimental data taken in the UT inlet.
5. Controllability analysis was conducted for advanced control theoretical solutions to regulate the shock wave's position. These theoretical efforts represent fundamental contributions to nonlinear control theory due to the fact that the control input signal arises non-affinely (nonlinearly) within the governing dynamics.

3.3.1 Actuator Comparison

To investigate strategies for achieving inlet/isolator unstart control the effects of Wheeler Doublets (WDs) [4], Vortex Generator Jets (VGJs) [5,6], and their combination on supersonic inlet unstart was explored for the UT inlet-isolator model described above. The objective was to achieve active control of unstart through the use of an unstart detection technique and the most effective of these actuators. To produce VGJs at the inlet, an air injection system connected to the injection ports in the inlet was used. The air was supplied to the jets by using four high-speed solenoid valves.

Based on the idea of energizing the isolator's sidewall boundary layers to prevent supersonic inlet unstart, the three vortex generating actuator configurations were tested. WDs were mini-ramps placed in pairs along the inlet's inner sidewalls, as shown in Fig. 8. The VGJs had a pitch angle (α) of 30° and a skew angle (β) of 60°. The location of the VGJs on the inner sidewalls of the inlet is shown in Fig. 9. High-speed Parker solenoid valves were used to supply nitrogen at 140 psig to the VGJs. These solenoid valves had a time response of 1 ms, which allowed the VGJs to be useful in short time scales such as those associated with the transient process of unstart (8 ms). After testing each of these three actuators and comparing their results to the baseline case, the following results were observed:

i. The comparison of the WDs to the baseline case (no actuators) showed that the computed normalized standard deviation of the back-pressure decreased from 2.40 to 1.03 (57%). This observation suggests that the use of WDs can enhance the inlet-isolator ramjet mode performance by stabilizing the flow.

ii. The most beneficial steady flow VGJs injection configuration found was one in which the top two injection ports from each sidewall were used. The use of the VGJs increased the mean back pressure by 15.8%, as compared to the baseline case at the same flap angle.

iii. The combination of WDs and steady-flow VGJs were even more effective than the VGJs alone, since the back pressure achieved before unstart was 35.6% higher than that for the baseline case.

iv. The WDs + VGJs combination configuration consistently was able to sustain started flow for a flap angle that normally caused unstart for the WDs only case as long as the VGJs were ON. This result proved that the WDs+VGJs were capable of preventing unstart for bounded pressure disturbances equivalent to a certain flap angle.

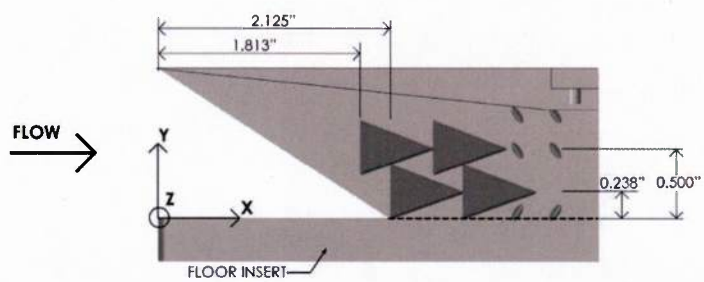

Figure 8. Dimensions of the vortex generator used to form Wheeler Doublets.

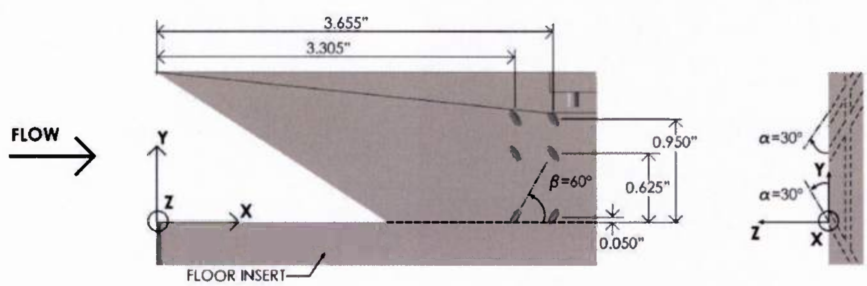

Figure 9. Schematics of the inlet instrumented for VGJs with 60° skewed and 30° pitched injection ports.

3.3.2 Active Control of Inlet Unstart

The control system can be divided into hardware and software. The control hardware was composed of seven pressure transducers (sensors), a control and acquisition system (National Instruments CompactRIO), and four high-speed valves. These components were connected to form a feedback control loop, in which seven pressure measurements were acquired simultaneously by the analog input module in the control/acquisition system at 100 kHz. These measurements then were processed by the control software programmed into the controller at 25 ns per decision and finally one digital output signal was transmitted to the Iota One Valve Driver to open or close the four high-speed Parker valves simultaneously.

The programming language used to code the control/acquisition system was National Instruments LabVIEW 8.2 and LabVIEW 8.2 FPGA, where FPGA stands for Field Programmable Gate Array. The main advantage of using Labview 8.2 FPGA and the CompactRIO system (containing an FPGA in its back plane) over other control devices and software configurations is the high processing speed of the FPGA at 25 ns per decision. The program used to control the high-speed Parker valves worked as a threshold control. The control program had the ability to detect when the supersonic inlet had become started and then turn the actuators on as soon as signs of unstart were detected.

Figure 10 shows the effect of periodic pulsed jet injection on the wall pressures inside the isolator. The figure shows that each transducer detects a rise in pressure while the jets are firing, except for the most downstream transducer that only responds to the jets once the flow is unstarted. This figure demonstrates that the jets create a large disturbance to the isolator flow that is readily detected.

The pressure traces just before unstart occurred were carefully inspected for signs of a precursor signal that could be used as part of a control scheme. These studies showed that the unstart shock system takes approximately 4 ms to go upstream from transducer T6 to T7 during unstart. It also was observed that the spikes in pressure at T6 were precursors of unstart when the flow in the inlet-isolator was marginally stable, namely when the flap angle was set high enough to induce unstart for the given inlet-isolator-actuator combination; therefore, the method used to detect unstart by the control system was based on the behavior of the pressure signal at T6.

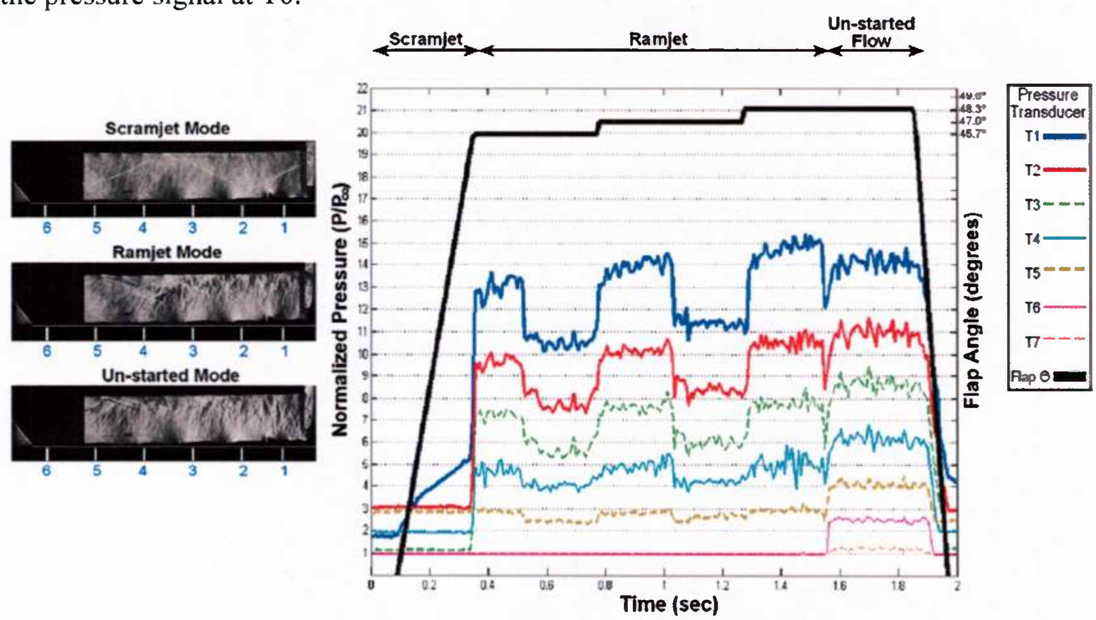

Figure 10. Inlet-isolator normalized pressure signals (*y*-axis left hand side) and flap angle (*y*-axis right hand side) as a function of time for WDs+VGJs case. Flap is raised from 45.7° to 48.3° in 1.3° increments. VGJs were ON at times *t* = 0, 0.75, and 1.275 s, and OFF at times *t* = 0.5, 1.05, 1.55 s.

Active control of unstart using the T6 precursor signal was tested several times for consistency. The results are shown in Fig. 11. In this test the flap angle was increased from 46.3° to 47.6° in steps of 0.3° and the WDs+VGJs actuator was used. Time histories of six wall pressures transducers along with the variation of the flap angle and the VGJs' activation signal are shown. Active control was achieved since unstart did not occur at any time during the run for flap angles that would always lead to unstart in the absence of control. It should be noted, however, that active control was successful in preventing unstart only about 50% of the time. The main reason that the control system was not capable of stopping unstart every time is that it took about 4 ms for the flow to respond to the VGJs, which was approximately the same time window that the controller had to stop unstart once it had detected it. The effectiveness of control should be improved by using a faster actuator or a better precursor to unstart.

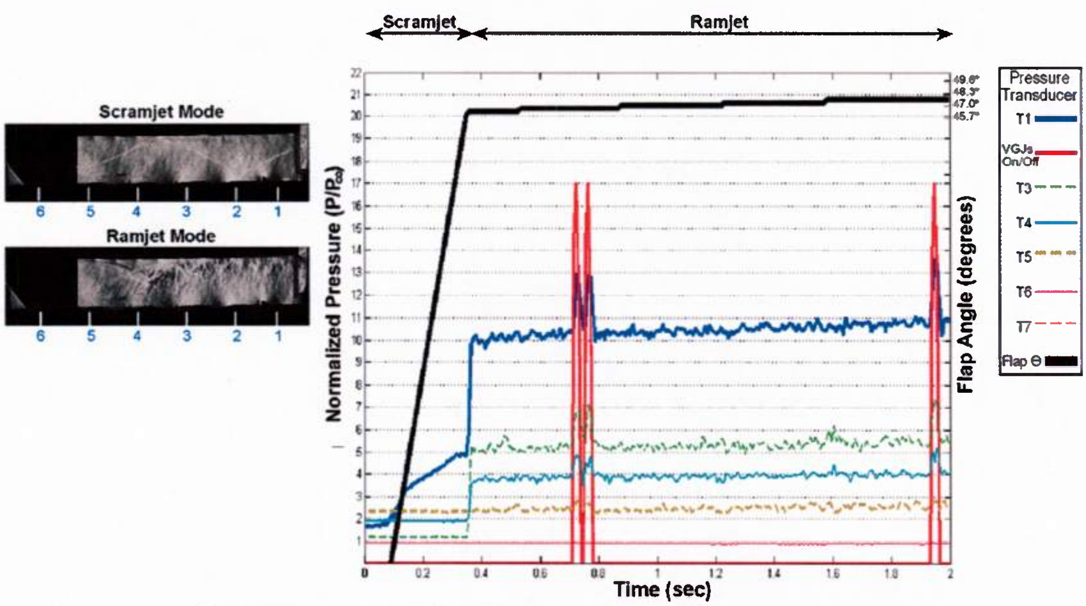

Figure 11. Active Control of Inlet Unstart with WDs+VGJs combination. Inlet-isolator normalized pressure signals (*y*-axis right hand side) and flap angle (*y*-axis right hand side) as a function of time.

3.3.3 Development of Adaptive Control Schemes for Unstart Prevention

Inlet unstart is a highly complex and nonlinear physical phenomenon in which the shock structure is displaced by disturbances both upstream and downstream of the inlet. As part of this overall research effort, we significantly built on to the existing body of work by creating new classes of low-order dynamic models of isentropic inlets with normal and oblique shocks. We had validated the dynamic characteristics of these models by comparing the predicted shock response to downstream perturbations using Schlieren data. Our research work also consisted of controllability analysis and advanced control theoretical solutions to regulate the shock wave's position. These theoretical efforts represent fundamental contributions to nonlinear control theory due to the fact that the control input signal arises non-affinely (nonlinearly) within the governing dynamics. The controller formulations included a PID controller, a "smooth" nonlinear feedback controller, and a dynamic nonlinear feedback controller. Additionally, our work focused on power spectrum analysis of experimentally obtained time-resolved transient pressure measurements during unstart and new designs for robust and adaptive feedback control with rigorous stability assurances in the presence of: (a) parametric uncertainties in the characterization of the dynamic model and (b) non-negligible time delays due to lags induced by signal processing and controller implementation. Specific details of this work are summarized below.

Given the input non-affine nature of the underlying dynamics model, adaptive control formulations must ensure sign-definiteness of parameter instantaneous time estimates to guarantee controllability for the overall controller implementation. While this objective in principle can be accomplished through classical projection schemes, given their non-smooth nature, those methods require high bandwidth, which poses a significant bottleneck from the standpoint of practical implementation. On the other hand, our work during the prior years led to the formulation of a new class of Wrapper Functions [7,8], which intrinsically involve low-pass filters. Given that the control signal also needs to be passed through the low-pass filters, these techniques, while theoretically rigorous, again have limited utility given the fast time-scales associated with the unstart process.

Motivated by the recent work of Ref. 9, we establish a model for the dynamics of moving oblique shock waves. The moving oblique shock wave dynamics are derived using singular perturbation techniques. This development led to following nonlinear differential equation, which models the motion of an oblique shock wave:

$$\frac{dx_s}{dt} = -\frac{a}{3} + \left(\frac{-2a^3 + 9ab - 27c + \sqrt{(2a^3 - 9ab + 27c)^2 + 4(-a^2 + 3b)^3}}{54}\right)^{\frac{1}{3}} + \left(\frac{-2a^3 + 9ab - 27c - \sqrt{(2a^3 - 9ab + 27c)^2 + 4(-a^2 + 3b)^3}}{54}\right)^{\frac{1}{3}}$$

wherein a, b, and c are constants related to the flow boundary conditions. Based on these low-order dynamics, numerical simulations for various inlet conditions were performed. The numerical simulation framework closely mimics the geometry and boundary conditions of a physical inlet model in the supersonic wind tunnel at the University of Texas at Austin. Figure 12 shows the response of the simulated inlet to step and sinusoidal disturbances.

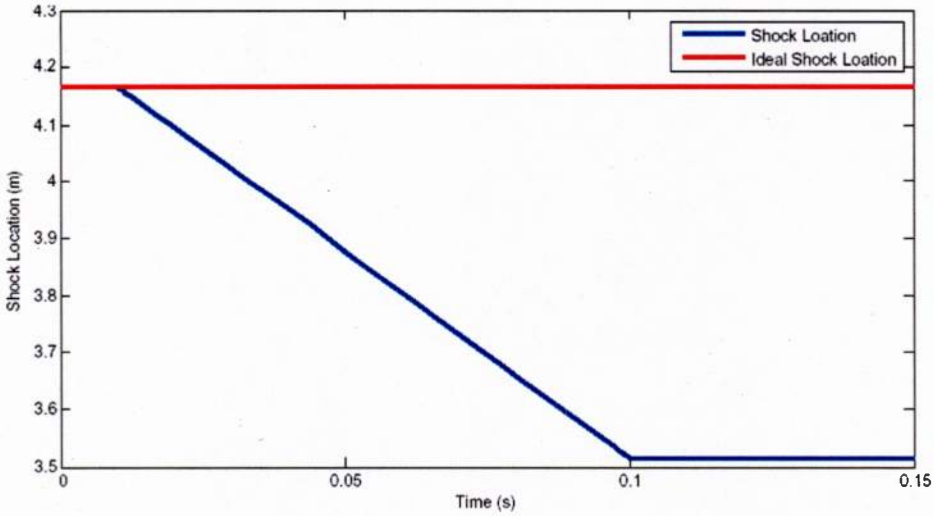

(a)

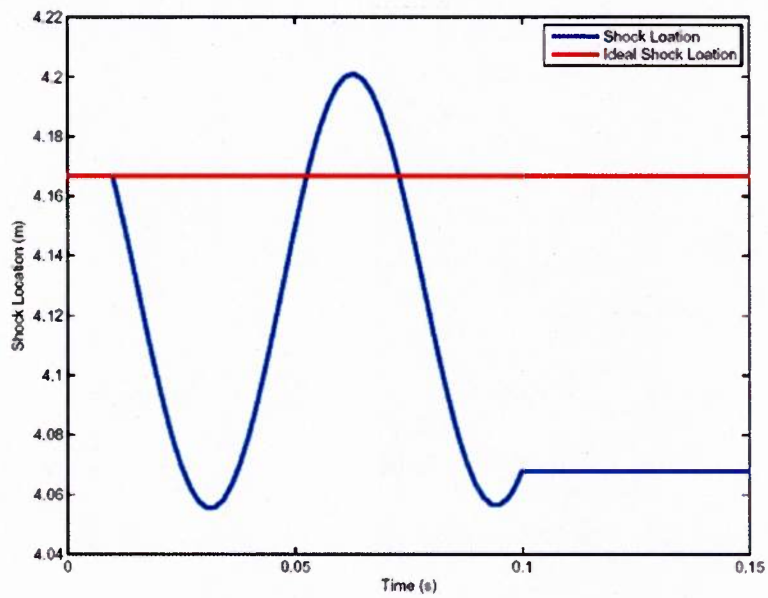

(b)

Figure 12. Uncontrolled response of the inlet: (a) response of the oblique shock structure to a step input, (b) response of the oblique shock structure to a sinusoidal input.

Figure 12(a) shows the response of the oblique shock structure to a step input started at T = 0.01 seconds and returned to nominal conditions at T = 0.1 seconds. Figure 12(b) shows the response of the oblique shock structure to a sinusoidal input with the same "on/off" conditions. Since the inlet is modeled as constant area, when the flow conditions return to nominal values, the shock structure does not return to the ideal location.

We invested extensive efforts in validating the new model describing the oblique shock structure dynamics. Validation was accomplished by analyzing experimental data obtained independently in the UT inlet experiment. The experimental data acquisition system is capable of obtaining Schlieren imaging of the inlet and pressure data along the length of the inlet. Unstart is simulated in the experiment by actuating a flap downstream of the inlet. Model validation is performed by comparing the shock position in the Schlieren imaging to that provided by the oblique shock dynamics model. Figure 13 depicts three cases under which the model was tested. The model validation cases are created using real pressure data from the wind tunnel, which are fed into the simulation. The model generally can predict the motion of the oblique shock structure to a very high degree of accuracy. The disturbances fed into the simulation are the actual "noisy" signals straight from the wind tunnel data. By filtering these signals, the simulation begins to do a better job of predicting the shock motion in the final two cases shown on the right in Figure 13. This validation study also confirms an observation widely seen in literature that decreasing the frequency of the disturbance causes the shock motion to become unstable and is, therefore, more likely to cause unstart.

Using the low-order singular perturbation dynamic model, the next major research thrust was analysis for controllability. Without an assurance on controllability, the development of suitable feedback control techniques would be impossible. Given the non-affine nature of control signals present within the governing dynamics model, we take the partial derivative of the shock wave dynamics with respect to the upstream velocity to investigate whether or not the value remains sign-definite ensures controllability. The partial derivative is taken with respect to the upstream velocity because this value is, in effect, the control variable though this value is changed indirectly by controlling the area ratio. Figure 14 shows a plot of the partial derivative, evaluated numerically. This plot is taken across a range of upstream Mach numbers ranging from 2 to 20 (this range was used to ensure that all possible inlet boundary conditions are covered).

We also have investigated the explicit effects of time delay in control implementation and closed-loop stability due to data processing and/or computational lags. In this process, new sets of sufficient conditions are established in terms of Lipschitz-type hypotheses [10,11] over the drift terms in the governing equations. These control strategies offer far greater sophistication and potential for superior performance compared to gain scheduling control or proportional control laws investigated in the past [12,13].

Experimentally determined and time-resolved pressure data were analyzed to investigate their potential for detecting the onset of unstart. More specifically, near the onset of unstart the standard deviation of the pressure data showed a distinctive amplification, especially for the case of upstream pressure taps. Likewise, the frequency content of the pressure signals exhibited certain unique characteristics during unstart. The experimental data were based on the inlet and constant area isolator model shown in Figure 15. Boundary layer pressure measurements from seven fast-response pressure transducers (Kulite XCQ-062-50A) recorded at 192 KHz over a 2 s window were used to determine the terminal shock location and hence predict onset of unstart.

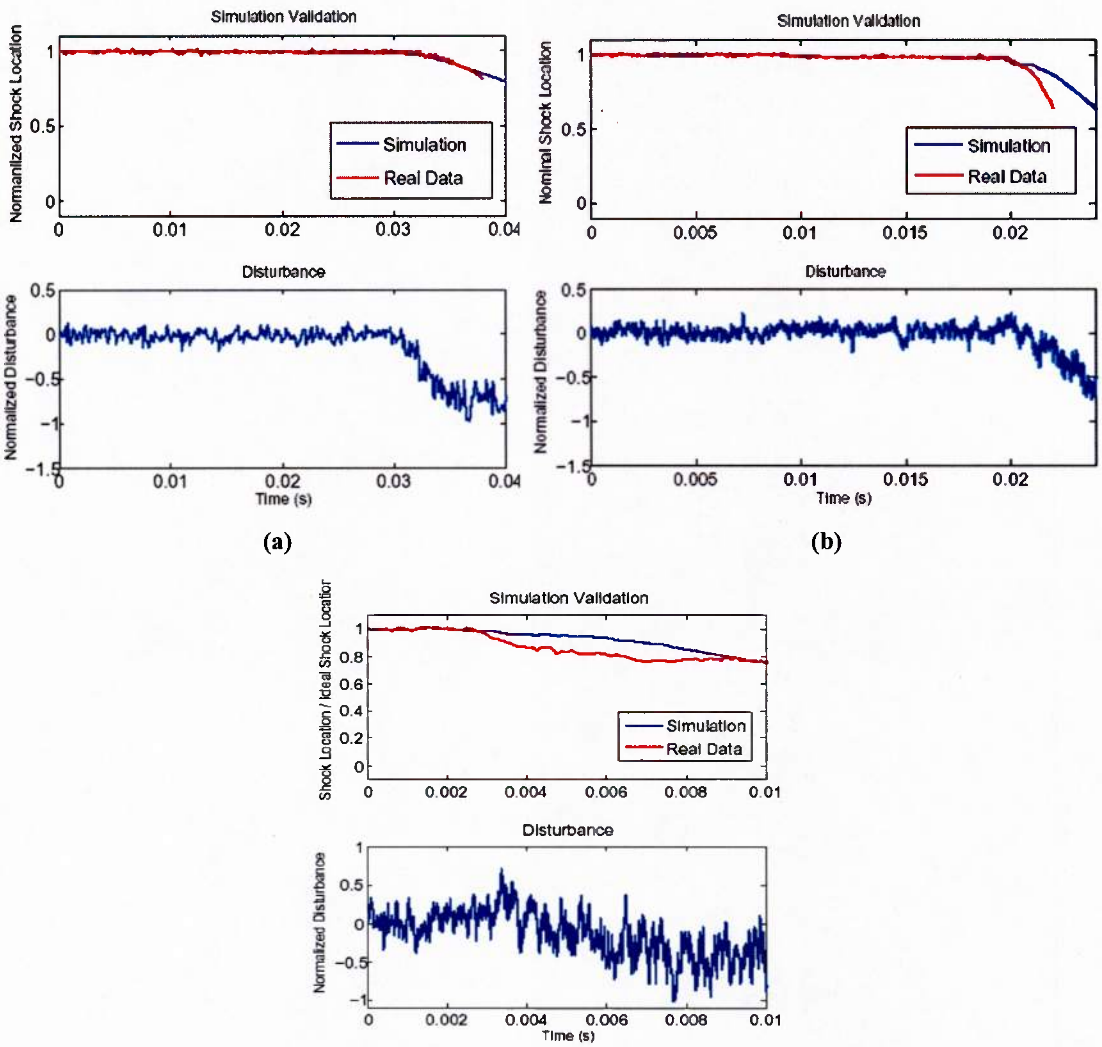

(c)

Figure 13. Validation of the Oblique Shock Dynamics Model used in the control system: (a), (b) and (c) are three independent examples showing the disturbance and shock-response waveforms.

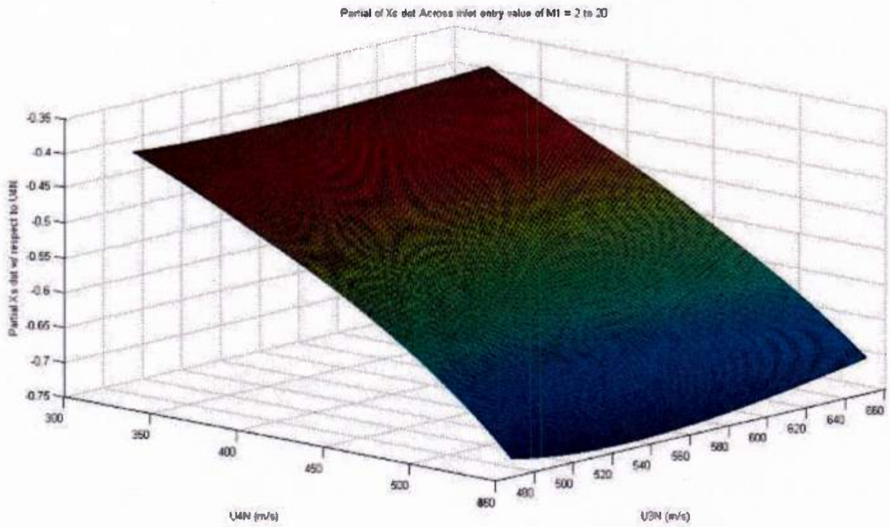

Figure 14. Controllability plot.

The flow conditions and the inlet/isolator setup result in a shock structure comprising an initial oblique shock and two subsequent reflected oblique shocks in the scramjet mode. As the system enters the ramjet mode of operation, a stronger oscillatory lambda shock system is formed downstream. At the onset of unstart the shock structure begins to move upstream and eventually is displaced upstream of the isolator into the inlet. The interaction of the shock structure with the pressure transducer is expected to change the behavior of pressure measurements relative to behavior upstream of the shock influence. This change forms the basis for the following shock edge detection criteria. Boundary layer pressure data can be used directly to detect the shock terminal edge location. The location is based on the pressure rise downstream of the shock terminal edge and can be seen in Figure 15. The figure shows that, at around t = 1.17 s, the shock passes upstream of taps T3, T6 and T7, which indicates ejection of shock structure from the inlet. As described above, we have explored pressure threshold-based detection on tap T6 as an indicator of the onset of unstart; therefore, for the purpose of comparison with standard deviation- and power spectrum-based techniques, we select a similar pressure threshold for tap T6 at 4.6 VDC (2.16 psia) and for the downstream tap T3 at 1.2 VDC (12.02 psia) by observing the trend in pressure data.

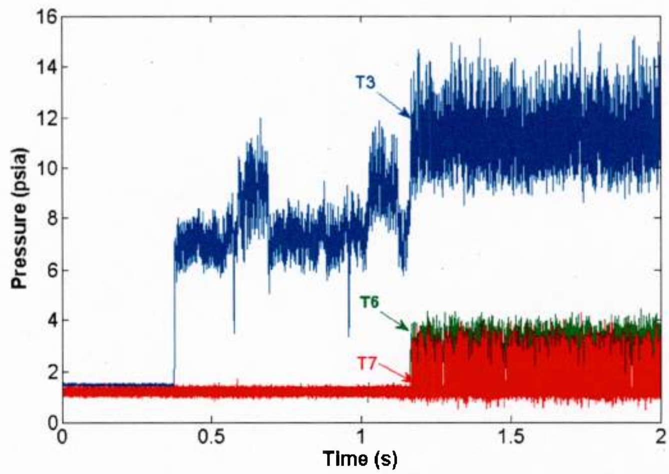

Figure 15. Pressure History Depicting Unstart.

The ramjet mode of operation introduces a stronger oscillatory lambda shock system close to the isolator exit. The impingement of the stronger shock structure on the downstream taps causes a surge in pressure, and the oscillatory behavior of the shock system increases the standard deviation of pressure. This phenomenon in the downstream tap T3 is clearly evident at around t = 0.35 s in Figure 15. Unstart happens when the lambda shock system reaches the upstream taps, after which it is disgorged from the inlet; therefore, an increase in the standard deviation of pressure in the upstream taps can be used as a reliable indicator of unstart.

Figure 16 confirms our theory for taps T6 and T7. Tap T3 does not show any clear characterization of the onset of unstart. This observation is expected, since T3 is already downstream of the edge of the lambda shock system in the ramjet mode, and so the onset of unstart does not change the standard deviation significantly.

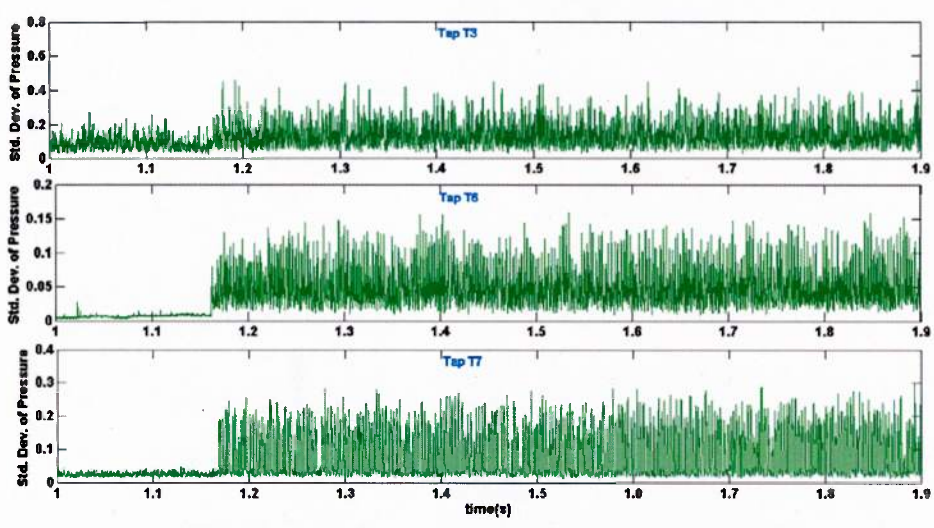

Figure 16. Standard Deviation of Pressure During Unstart.

We have developed an automated algorithm that can be implemented in real time to utilize this jump in standard deviation to detect the onset of unstart. The algorithm takes, as input, the pressure data, and computes the baseline standard deviation (h) based on an initial sampling time (t_0). Beyond this initial sampling time the standard deviation is computed over a moving smoothing window (w). The value of the standard deviation after each window (w) then is compared with the threshold value (h_{max}) expressed as a function of the baseline value. If the algorithm determines that the standard deviation exceeds the threshold for a majority of the unstart detection windows (w_u), then the algorithm declares that unstart has occurred. These parameter values were optimized based on reliability of detection and chosen as shown in Table 1 below. The delay introduced in unstart detection due to the algorithm stems from the unstart detection window size and is equivalent to approximately 1.56 ms (300 sample points).

TABLE 1. PARAMETER SELECTION

Initial sampling time, t_0	0.01 s
Smoothing Window, w	500 points ≈ 2.6 ms
Threshold, h_{max}	1.5h + 0.02
Unstart Detection Window, w_u	300 points

Power spectrum-based detection relies on frequency domain characteristics of the wall-pressure measurements. We have documented a distinct amplification in the 300-400 Hz band around unstart. We seek to exploit this sudden rise in energy distribution across frequencies to predict the onset of unstart. The sensitivity of the power spectrum was analyzed based on the following definition,

$$Sensitivity = \frac{Max. Power\ in\ Frequency\ Band\ During\ Unstart}{Max. Power\ in\ Frequency\ Band\ Before\ Unstart}$$

The following observations were made based on the sensitivity analysis of the pressure data in the 1-1000 Hz band divided into 100 Hz windows:

i. The downstream taps show lower sensitivity for all frequencies compared to the upstream taps.
ii. The highest sensitivity in the 300-400 Hz band occurred for the downstream taps, whereas the highest sensitivity in the 1-400 Hz band occurred for the upstream taps.
iii. No amplification within the frequency bands was seen in runs where there was no unstart.

The algorithm implemented is very similar to the standard deviation-based detection algorithm except that, instead of the standard deviation, we compute the power spectrum in 300-400 Hz band for the downstream tap T3 and the power spectrum in 1-400 Hz for the upstream tap T6. The chosen parameter values are tabulated below in Table 2.

TABLE 2. PARAMETER SELECTION

Initial sampling time, t_0	0.03 s
Smoothing Window, w	6000 points ≈ 31.25 ms
Threshold, h_{max}	2.5h + 4500
Unstart Detection Window, w_u	10 points

The power spectrum computation is modified in order to reduce computation time for real-time implementation. The delay introduced in unstart detection due to the algorithm stems from the unstart detection window size and is equivalent to approximately 0.05 ms (10 sample points).

The unstart detection times, as predicted by each detection algorithm described above, is tabulated in Table 3. The data are based on 8 different runs, 2 of which are runs with no unstart (427 and 440). "NA" in any entry of the table indicates that no unstart was detected by the algorithm. The power spectrum-based detection scheme is denoted as "FFT" and the standard deviation-based detection scheme is denoted as "STD."

TABLE 3. UNSTART DETECTION TIMES

RUN	TAP T2/T3 (DOWNSTREAM)			TAP T6 (UPSTREAM)		
	FFT	**STD**	**Pressure**	**FFT**	**STD**	**Pressure**
427	NA	1.2370	NA	NA	NA	NA
430	1.2139	1.1829	1.2074	1.1800	1.1726	1.2054
433	1.1800	1.0486	1.1691	1.1635	1.1628	1.1627
435	1.7172	1.3519	1.716	1.7123	1.3442	1.7112
436	1.2142	1.4776	1.2070	1.2008	1.1997	1.2002
438	1.7406	NA	0.3868	1.7145	1.4364	1.7224
440	NA	NA	0.3717	1.6872	1.2855	NA
442	1.3597	NA	0.3419	1.0750	1.0663	1.3483

The following conclusions can be drawn based on results reported under Table 3:

- Both the pressure threshold and STD criteria usually have difficulty with unstart prediction using downstream taps.
- The pressure threshold criterion generally predicts unstart earlier in downstream taps, but the results using the FFT method are comparable and often better.
- The STD method gives a greater number of false detections compared to the other two methods.
- The FFT technique is usable both on upstream and downstream taps. Although there is no observable improvement in detection times for the present set of runs it may be a more reliable technique for detecting unstart.

A most important contribution of this research has been to show the feasibility and advantages of spectral analysis for unstart detection, which is a significant improvement over previous work. Implementation of the power spectrum-based detection using analog band pass filters can be explored to cut out processing time significantly.

3.4 Plasma Actuator Modeling and Development (PIs: Raja, Clemens)

This section reports the progress made towards computational modeling and experimental development of surface plasma actuators for high-speed flow control applications. The primary objective of this work is to obtain physical insight into the discharge structure, chemical composition, and energy deposition pathways of a surface plasma discharge in the presence of a supersonic air flow using computational models to gain a better understanding of high-speed plasma actuators. The experimental work was aimed at demonstrating that sufficient actuation authority of a plasma actuator can be achieved to control the unsteadiness of a shock wave/boundary layer interaction. The major accomplishments of this work are summarized as follows:

1. Development of a new self-consistent, multi-species, multi-temperature, finite-rate chemistry continuum description of plasma discharges.
2. Coupling of the plasma model to a supersonic flow code
3. Accurate prediction of the effect of DC glow discharges in supersonic flows and validation with experiments in a Mach 3 wind tunnel.
4. Development and characterization of a pulsed plasma jet actuator that operates at rates as high as 5 kHz.
5. Application of a pulsed plasma jet actuator to control the unsteadiness of a Mach 3 shock wave/boundary layer interaction.

3.4.1 Plasma actuator modeling

To model multi-dimensional glow discharge phenomena in air under typical actuator operating conditions, there is need for establishing a plasma chemical reaction mechanism that is capable of representing all important finite-rate chemistry effects in a non-equilibrium air plasma; however, the plasma chemistry must be reduced sufficiently to enable feasible multi-dimensional computational simulations. The plasma model used in the present work is based on a self-consistent, multi-species, multi-temperature, finite-rate chemistry, continuum description of the plasma. A reduced air plasma model suitable for multi-dimensional applications with 11 species and 21 gas-phase chemical reactions was developed and validated using experimental results from the literature [14].

The air plasma chemistry model is found to provide reasonably good prediction of experimental spatial profiles of the electron temperatures, positive ion number densities, and current-voltage characteristics of the discharge, as shown in Figs. 17 and 18. For pressures of order 1 Torr, O_2^+ and N_2^+ are the dominant positive ion species in the discharge, and the concentration of O^- is comparable to electron concentration. The air plasma therefore can be characterized as moderately electronegative. The two-dimensional structure of the discharge obtained from the computations is found to be in agreement with qualitative observations from the experiments.

The present air plasma model is self-consistently coupled to a compressible Navier-Stokes solver to study the effects of the surface plasma on supersonic flow and the effect of the flow on the discharge structure. The typical surface plasma actuator device length is ~1 cm, and the plasma discharge is confined to a region a few mm above the surface; however, the length scale associated with the flow could be several centimeters long, and solving the plasma model on the entire domain is neither feasible nor required for localized surface discharges in the present study. Hence, a combined numerical model of the supersonic flow and the plasma has been developed, with the ability to solve the plasma model on localized subdomains that are a subset of the overall simulation domain. On the localized subdomains both the plasma and Navier-Stokes models are solved using an iteratively decoupled algorithm. The source terms are exchanged between the two models in each combined iteration. The bulk flow field pressure, velocity, and gas temperature from the Navier-Stokes solver are used as inputs to the plasma model, and electrostatic force (momentum source) and

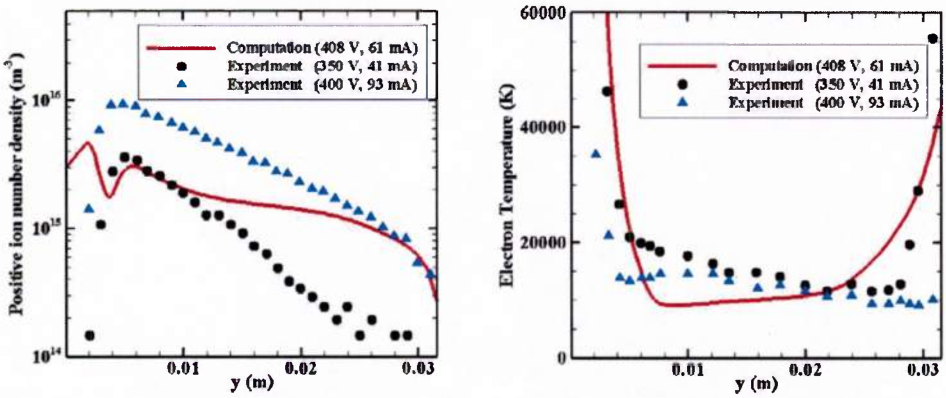

(a) Positive Ion Density (m^{-3}) (b) Electron Temperature (K)

Figure 17. Comparison of (a) axial total positive ion number density and (b) axial electron temperature with experimental measurements [14]. The inter-electrode distance is 32 mm, the applied voltage is -350 V and the discharge pressure is 600 mTorr.

volumetric heating (energy source) terms from the plasma model are used as inputs to the Navier-Stokes solver.

The species concentrations and the gas temperature are examined in the absence and presence of bulk supersonic flow. Fig. 19 shows the electron density contours in (a) the absence of supersonic flow and in the presence of supersonic flow with the cathode located (b) upstream and (c) downstream with respect to the flow direction. In the presence of supersonic flow, the discharge is swept downstream due to convective effects. The peak gas temperature from the computations is found to be 1180 K with the surface plasma alone, 830 K in the presence of supersonic flow with the cathode upstream, and 620 K with the cathode located downstream with respect to the freestream flow direction. Gas heating is the predominant actuation mechanism, and the effect on the flowfield is a weak shock above the cathode surface, as seen in Fig. 20. The cathode upstream actuation is found to be stronger than the actuation strength with the cathode downstream, which is consistent with our experimental findings.

The O^- concentration is found to exceed the electron concentration in the pressure range 1-20 Torr, and O_2^- concentrations are at least two orders of magnitude smaller over the pressure range considered. The fact that the plasma is electronegative under the present conditions and the electronegativity has a strong influence on the discharge potential and electron temperature profiles indicates that a pure nitrogen plasma model is not a good surrogate for an air plasma model [14].

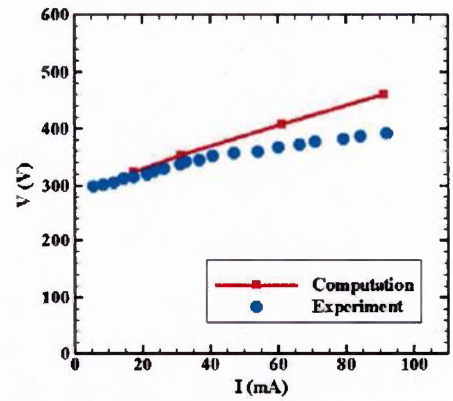

Figure 18. Comparison of V-I characteristic obtained with the model and experiment [14]. The inter-electrode distance is 32 mm and the discharge pressure is 600 mTorr.

The dominant positive ion species in the cathode sheath is N_2^+, while O_2^+ is the dominant positive ion species in the bulk plasma when no supersonic flow is present. With supersonic flow, O_2^+ and O_4^+ are found to be the dominant positive ion species in the bulk plasma, while N_2^+ remains dominant in the cathode sheath. Hence, different ion species are found to be dominant in the absence and presence of supersonic flow, highlighting the importance of including finite-rate chemistry effects in discharge models for understanding plasma actuator physical phenomena.

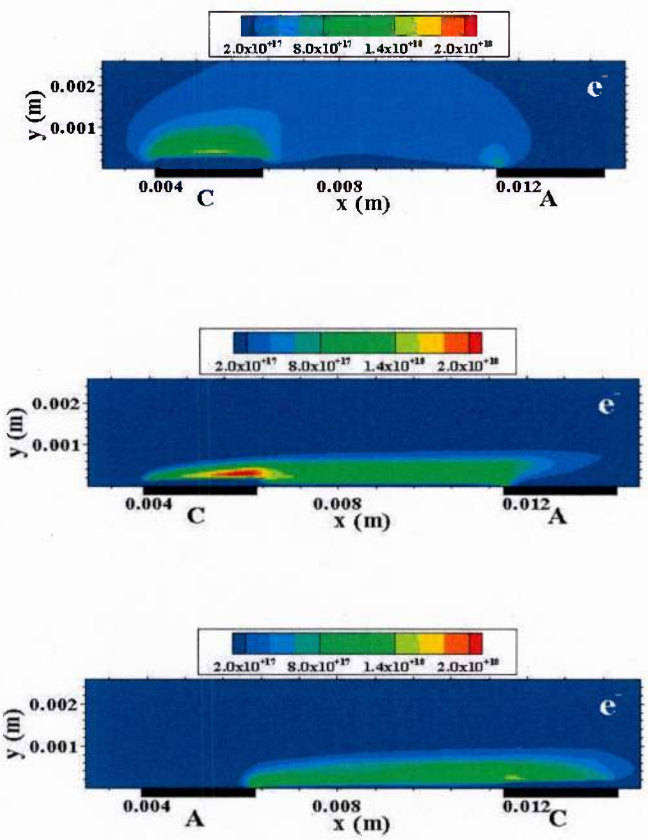

Figure 19. Contours of the electron number density (m^{-3}) (a) with no flow and in the presence of M=3 supersonic flow with the cathode located (b) upstream and (c) downstream. The flow is from left to right, the cathode source voltage is -1000 V, and the static pressure is 18 Torr.

In practice, the highly disparate time scales (ranging from 10^{-11}-10^{-9} s for electrons to 10^{-5}-10^{-4} s for the ion diffusion and supersonic flow time scales) and the corresponding long integration times to obtain a steady-state solution lead to practical limitations on the computational grid size and the chemistry model. Importantly, the actuators in practice have circular pin-like electrodes, which make the problem three-dimensional and thus too computationally time consuming with our current serial code. A parallel implementation of the plasma and flow models therefore was developed as part of this research. The parallel model was used to study the three-dimensional plasma actuator configuration with circular pin electrodes in the absence of bulk supersonic flow. Fig. 21 shows the three-dimensional structure of the discharge in the pin electrode configuration, solved on 128 processors. For the same operating conditions as the previous two-dimensional cases, the discharge is formed above the circular cathode surface, extending through the bulk plasma and attached to the leading edge of the anode. In general qualitative agreement is found between the three-dimensional and corresponding two-dimensional simulations for the same operating parameters.

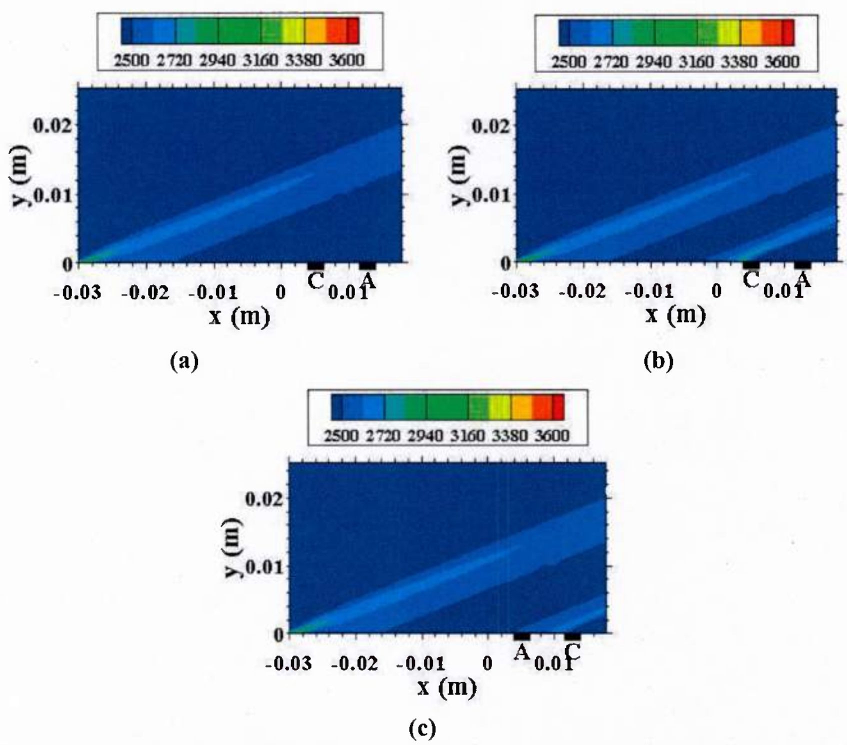

Figure 20. Pressure (Pa) contours with the plasma (a) off, and plasma on with the cathode located (b) upstream, and (c) downstream with respect to the supersonic flow. The leading edge shock is seen along with a shock above the cathode.

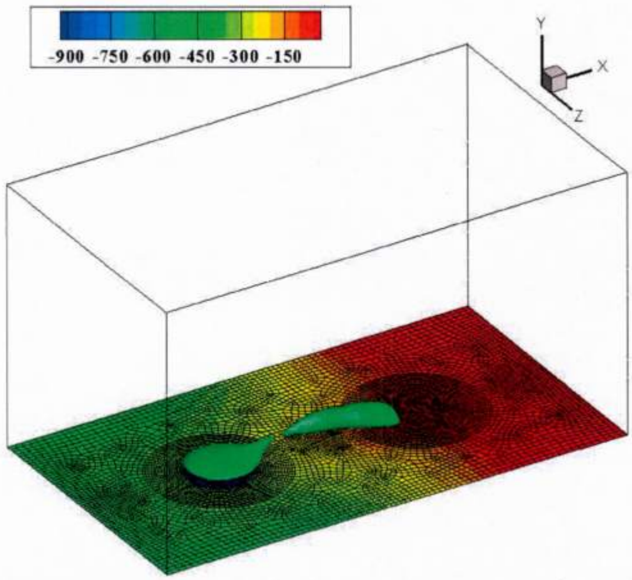

Figure 21. Three-dimensional structure of the discharge in the pin electrode configuration, The isosurface of O_2^+ at a value of 2.8×10^{18} m^{-3} is shown. Contours of the potential (V) on the electrodes and the dielectric surface are also shown.

3.4.2 Actuator Development - Pulsed Plasma Jet for High-Speed Flow Control

Several different actuator configurations were tried during the course of this research program, but most of the work was directed at glow discharges and pulsed plasma jets. The pulsed plasma jet held the most promise for supersonic flow control, so this actuator will be detailed here. The plasma jet first was developed at the Johns Hopkins' Applied Research Laboratory but had not been shown to be effective in supersonic flows. The principle of operation of the plasma jet is the rapid expansion of gas in an enclosed chamber caused by sudden deposition of thermal energy through electric discharge. The expanding gas is allowed to issue through an orifice of suitable dimensions. Figure 22 shows a schematic of the experimental setup.

The discharge was achieved by rapidly switching a high-voltage across the electrodes in the cavity by using a MOSFET switch. The switch remained closed for about 20 µs. The rapid energy deposition caused rapid heating of the air inside the chamber. The heating is determined by the discharge current that is controlled, in turn, using a ballast resistor. Pulse width and frequency were set using a BNC signal generator, and frequencies up to 5 kHz have been tested. The typical velocity of the contact surface of the jet for a current of 1.2 A was measured to be about 250 m/s. At 8 A discharge current this velocity was about 400 m/s.

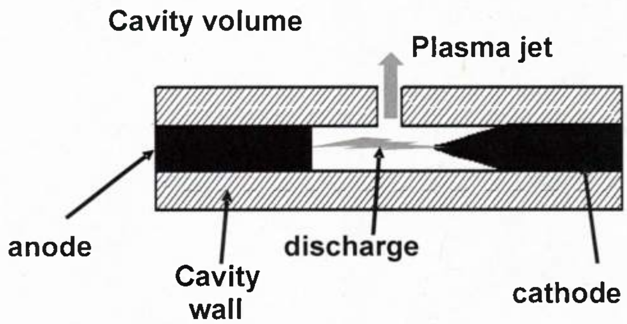

Figure 22. Schematic of the pulsed plasma synthetic jet device for high-speed flow control.

The effect of the pulsed jet array on a shock wave/boundary layer interaction generated by a 30-degree ramp was studied using 10 kHz schlieren imaging. An array of three pulsed plasma jets, pitched at 45° and skewed at 90°, was employed. The pulsing frequency of the jet was set at 1 kHz. For the present flow conditions the incoming boundary layer was fully turbulent with Re_θ=5000. The jet was injected at about 6δ from the ramp corner. Figure 23 shows a sequence of four images that show the separation shock motion as the disturbance due to the pulse plasma jet passes through the shock. Each image in the sequence is separated from its neighbors by 100 μs. Arrow (1) points to a line that indicates the shock position in frame Fig. 23(a), and arrow (2) shows the location of the perturbed shock location.

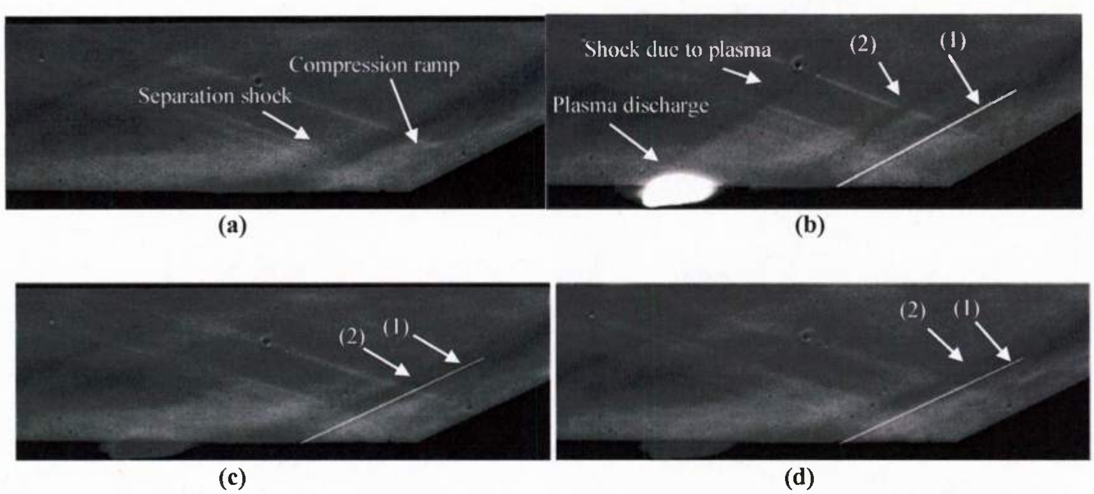

Figure 23. Time sequence of Schlieren images showing the effect of the pulsed-plasma jet firing upstream of the shock / boundary layer interaction. The flow is left to right. (a) t=0, (b) t=100 μs, (c) t=200 μs, and t=300 μs.

While the plasma array is firing, the separation shock moved about 1δ upstream, which is a significant amount. Since the discharge duration is only 20 μs, the discharge is over by Fig. 23(c), and the flow largely recovered by that time. A careful viewing of the movie sequences shows that it takes about 100μs before the separation shock recovers to its average undisturbed position. At 5 kHz pulsing frequency the separation shock never recovered to its undisturbed location, and it seemed to reach a quasi-steady upstream shift. This effect is evident in the movies but is difficult to see in the limited time sequences, so the images are not shown here. Another observation that can be made by carefully viewing the movies is that a brief (≈ 5 μs) downstream motion of the separation shock foot preceded the upstream motion. The downstream motion, which is not shown in the sequence above, was about 0.2 δ in extent. This initial downstream motion appears consistent with the actuator acting as a vortex generator that energizes the boundary layer and makes it more resistant to separation.

Planar laser scattering using condensed CO_2 also was carried out to study the response of the separated flow as the plasma-jet fluid passes through it. These image data show that the pulsed plasma jet strongly influences the scale of the separated flow as it convects into the interaction.

These results show that the pulsed plasma jets cause a large perturbation to the Mach 3 flow and are a very promising candidate for a high-speed flow control actuator.

3.5 Expansion Tube Development and Study of Supersonic Combustion (PIs: Mungal, Hanson)

The main objective of this work was to develop an expansion tube impulse facility for the investigation of fundamental aspects of ignition, stability, and combustion characteristics of transverse jets in high-enthalpy crossflow. The major achievements of this topic are summarized as follows:

1) Construction of the expansion tube facility for the investigation of high-enthalpy supersonic flows.
2) Investigation of the ignition and stability characteristics of transverse jets in supersonic crossflow (using hydrogen and ethylene as fuels).
3) Investigation of reaction zone structure of reacting hydrogen transverse jets in crossflow using OH PLIF imaging. The effect of freestream conditions and injection configuration were investigated.
4) Development of a tunable diode laser (TDL) H_2O absorption diagnostic for the time-resolved measurement of path-integrated gas properties, including static temperature and velocity.

3.5.1. Development of the expansion tube facility

The primary goal and achievement of the project was the design, construction, and characterization of the Stanford Expansion Tube. An expansion tube is a hypersonic impulse facility capable of generating a wide range of aerothermodynamic conditions necessary for the study of supersonic combustion, although at the expense of short test times [15]. The primary characteristics of the expansion tube are summarized briefly below.

Fig. 24 shows a photograph of the expansion tube developed as part of this work. A schematic diagram of the expansion tube and a typical (*x*,*t*) diagram (*x* is the distance along the expansion tube, *t* indicates time) summarizing the important processes occurring during the operation of the facility are shown in Fig. 25. The expansion tube is composed of three sections: a driver and a driven and expansion sections. The expansion section terminates into the test section open onto a vacuum dump tank. A suitable test model is secured within the test section. The three sections are separated by diaphragms and are pressurized independently with different gases of interest. The driven section contains the working fluid of interest ("test gas" that is typically room air). The test gas is processed to the desired thermodynamic state and set in motion by the combined effects of the primary shock (state 1 to 2 in Fig. 25) and the secondary unsteady expansion originating at the secondary diaphragm upon its rupture (state 2 to 5 in Fig. 25). The pressure (*p*), temperature (*T*) and Mach number (*M*) in the test section can be set independently by properly adjusting the filling pressures of each section without any major modification of the facility. An advantage of this facility over similar ones is that the expansion tube was designed in a modular fashion: the length of each section can be modified easily to optimize its performance over a wide range of equivalent flight conditions.

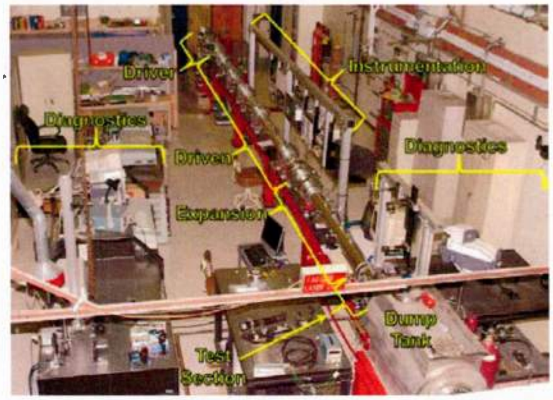

Fig. 24. Photograph of the expansion tube.

During the first period of the project the performance of the developed facility was investigated. Two criteria were considered important for the goals of the project: the capability of obtaining the desired conditions for supersonic conditions and their repeatability. We verified using different calibration procedures that the developed expansion tube is capable of reproducing the sought freestream conditions to within 1%. Fig.26

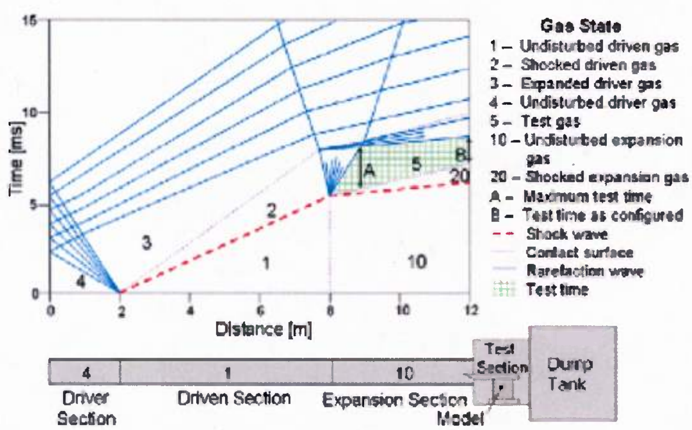

Figure 25. Schematic diagram of a typical expansion tube and corresponding *x-t* (distance-time) diagram showing the relevant processes occurring during the operation of the facility.

demonstrates the range of operation of the facility in terms of equivalent flight conditions. In determining these conditions it was assumed that a typical inlet process reduces the flow Mach number by a factor of 3. The flight corridor (flight altitude versus flight Mach number) of a hypothetical hypersonic vehicle is defined by the grayed area, and it is assumed to be bounded by the $q = 25\ kPa$ and $q = 100\ kPa$ lines, where q is defined as the dynamic pressure. The lower limit is determined by the need of providing sufficient lift and mass flow rate to the combustor, whereas the upper limit is determined by structural limitations [16]. The demonstrated range of operation is well within this flight corridor.

3.5.2. Flame ignition and stability of hydrogen jets in supersonic crossflow

An underexpanded sonic jet issued from a flat plate normal to a crossflow was selected as a basic flow configuration to investigate the ignition characteristics. As shown in Fig. 27, the flow around a jet in supersonic crossflow is characterized by a complex system of recirculation and stagnation regions along with a complex shock/expansion wave system, where the stagnation and recirculation regions might be important features for ignition and flame stabilization. The fundamental parameters determining the system are the freestream pressure, temperature, and Mach number. Furthermore, the jet-to-crossflow momentum ratio $J = (\rho u^2)_{jet}/(\rho u^2)_\infty$ (where the subscript "∞" indicates freestream conditions) describes the overall structure of the jet in crossflow.

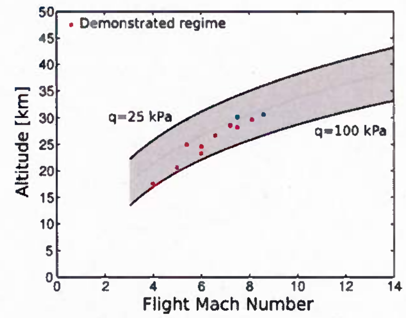

Figure 26. Demonstrated range of operation of the constructed expansion tube.

Taking advantage of the high enthalpy of the crossflow generated in the facility and the wide range of conditions of operations that the facility provides, we first systematically mapped the combustion stability limits of this fundamental flow configuration. A three-dimensional grid of test gas properties configured around cases roughly corresponding to scramjet combustor conditions at flight Mach numbers 8 and 10 was investigated. The static pressure was held constant at 25 kPa, and the stagnation temperature T_0 was varied from T_0 = 2300 K to 3100 K in 100 K increments for each of three static temperatures T = 1250 K, 1375 K, and 1500 K. Each freestream condition combination was tested with hydrogen injected at a jet-to-crossflow momentum ratio of J = 4, with some cases tested at J = 1 and 2. The principal diagnostic techniques were Schlieren imaging and planar laser-induced fluorescence (PLIF) imaging of the hydroxyl radical (OH). Combustion stability was defined based on the appearance of the overall structure and contiguity of the flame sheet, as revealed by the OH PLIF imaging. Flows

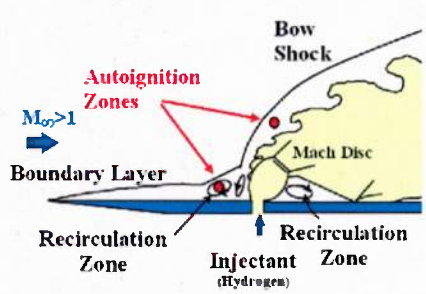

Figure 27. Schematic diagram of the sonic hydrogen jet in supersonic crossflow

were classified as stable (Fig. 28a), unstable (Figs. 28b-c), and no combustion (Fig. 28d). Fig. 29 summarizes in graphical form the (T, T_o) regions (at constant p and J) of stable, unstable, and no-combustion conditions. For the selected (p, J) conditions, the results indicate that the unstable/stable combustion boundary lies just over T_o = 2600 K for T = 1250 K, and the T_o value for stable combustion increases with increasing freestream static temperature T, going from about 2650 K for T = 1375 K to about 2750 K for T = 1500 K. The no combustion/unstable combustion boundary lies just under T_o = 2200 K for T = 1250 K and similar to the stable/unstable combustion boundary, T_o where no combustion is observed increases with increasing freestream static temperature. This somewhat counterintuitive result is believed to be due to the increase in the Mach number that is required to maintain a constant T_o while lowering T. An increase in Mach number, in fact, would generate stronger stagnation regions with higher stagnation pressure at the location of autoignition. An increase in stagnation pressure in turn would decrease the ignition times and, hence, increase flame stability. The values of stagnation temperature that are required for stable combustion are somewhat higher for lower J as a result of a decrease in the strength of the stagnation regions.

In addition to hydrogen, hydrocarbon fuels (methane and ethylene) also were investigated with the intent to provide a mapping of combustion similar to the one produced for hydrogen; however, the boundary between no combustion and unstable combustion for both ethylene and methane at J = 4 lies above T_0 = 3400 K for T = 1500 K and P = 25 kPa, which was the highest energy case available to be tested (ethylene was heated at about 400 K to avoid condensation during injection). Even at this high energy, both fuels showed only a very weak reaction at the autoignition point located where the freestream stagnates on the front of the jet. In practical terms, these results indicate that some stabilization mechanism (cavities, plasmas, pylons, etc.) must be used to enable combustion at lower stagnation temperatures corresponding to more realistic scramjet configurations.

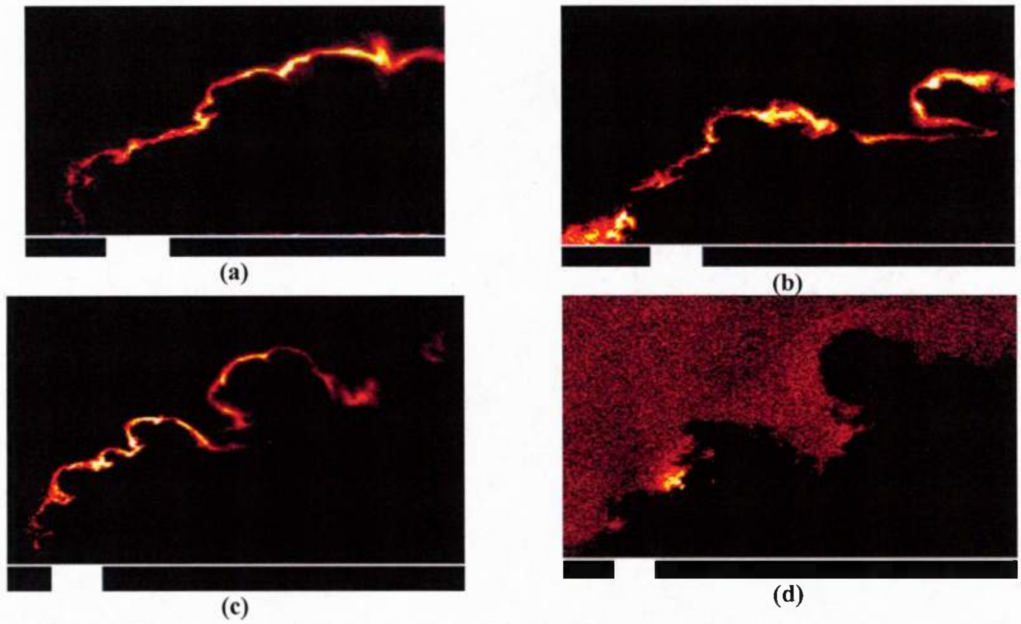

Figure 28. OH PLIF images of various regimes of burning: (a) strong combustion of hydrogen at T_0 = 2600 K, T = 1250 K, P = 25 kPa and J = 4 (b) discontinuous combustion of hydrogen at T_0 = 2900 K, T = 1500 K, P = 25 kPa and J = 2.9, (c) combustion of hydrogen with extinction at T_0 = 2600 K, T = 1250 K, P = 25 kPa and J = 4, and (d) no combustion of ethylene at T_0 = 3400 K, T = 1375 K, P = 25 kPa and J = 4. In (d) the display histogram has been adjusted to reveal the signal in the freestream from burning diaphragm debris, which, in contrast with the absence of signal from the clean injected gas, clearly indicates the fuel/freestream boundary. The unsteady bow shock also is revealed. The jet diameter and plate surface in each image are as marked, and all images are corrected for incident laser sheet intensity.

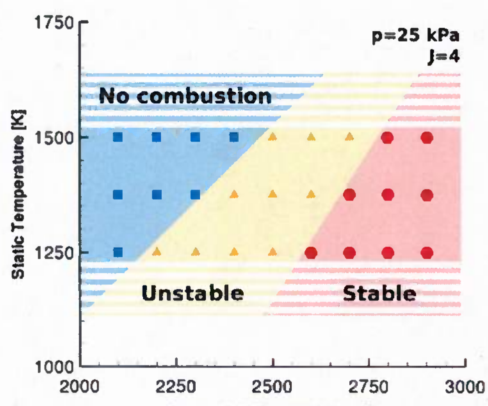

Figure 29. Combustion stability regimes for a hydrogen jet in crossflow at fixed pressure p = 25 kPa and J = 4.

3.5.3. Reaction zone structure of reacting hydrogen jets in supersonic crossflow

The third objective and achievement of the work was the investigation of the structure of the combusting hydrogen jet and the role of injection configuration (injection angle with respect to crossflow). The primary finding was the identification of the strong entrainment, mixing, and combustion within the incoming boundary layer initiated at the upstream recirculation region and affected by the interaction with the bow shock (see Fig. 27). OH PLIF imaging of multiple views on orthogonal planes was used to map the spatial features of the reaction zone. Hydrogen was used as fuel at J = 2.4 and J = 4.7. Two stable conditions (T = 1500 K, T_o = 2800 K, M = 2.4 and T = 1250 K, T_o = 2700 K, M = 2.75) were selected and considered throughout the experimental campaign. The freestream pressure was held constant at about 40 *kPa*. Injection angles (defined with respect to the crossflow direction) of 90°, 60° and 30° were considered. With reference to the coordinate system shown in Fig. 30, several side- (*x-y* plane), plan- (*x-z* plane) and end- (*y-z* plane) views were considered. The origin of the coordinate system is centered on the jet exit centerline.

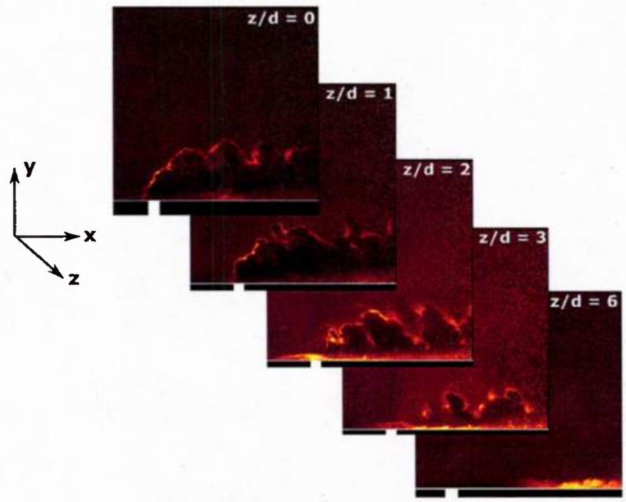

Figure 30. Side-views on several x-y planes (at different *z/d* locations) of sonic hydrogen injected into supersonic crossflow (M = 2.4) at *J*= 4. Freestream conditions are *T* = 1500 K, T_o = 2800 K, *p* = 40 kPa. *d* indicates the jet exit diameter (*d* = 2 mm).

Fig. 30 shows a composite image of the reaction zone structure as viewed by OH PLIF on several side-view planes at z/d = 0, 1, 2, 3 and 6 (d = 2 mm is the jet exit diameter). The case shown in the figure refers to the transverse (90°) hydrogen injection at J = 2.4 and freestream conditions of T = 1500 K, T_o = 2800 K (M = 2.4) and p = 40 kPa. Similarly, Fig. 31

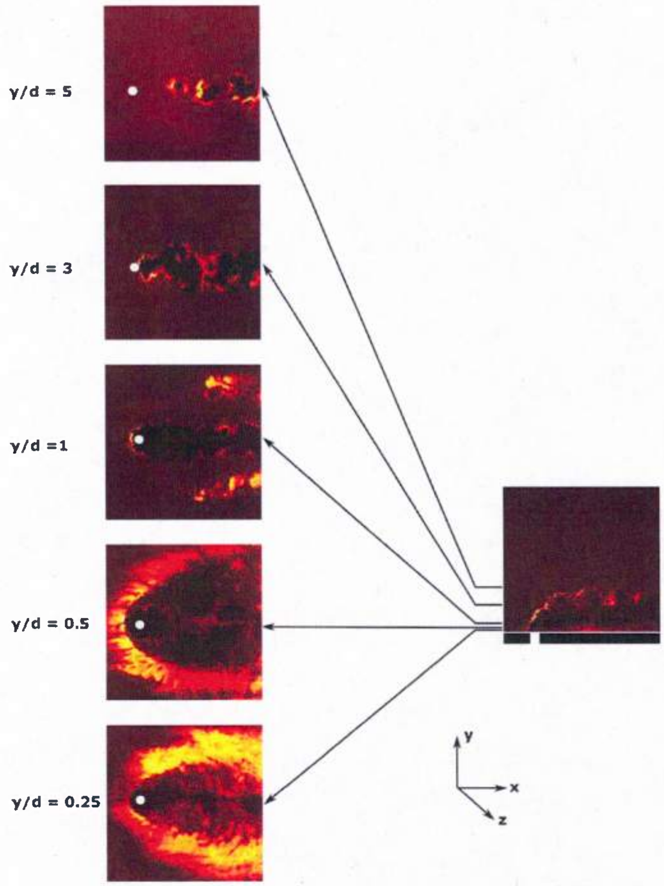

Figure 31. Plan views on several x-z planes (at different y/d locations) of sonic hydrogen jet injected into supersonic crossflow (M = 2.4) at J = 2.4. Freestream conditions are T = 1500 K, T_o = 2800 K, p = 40 kPa.

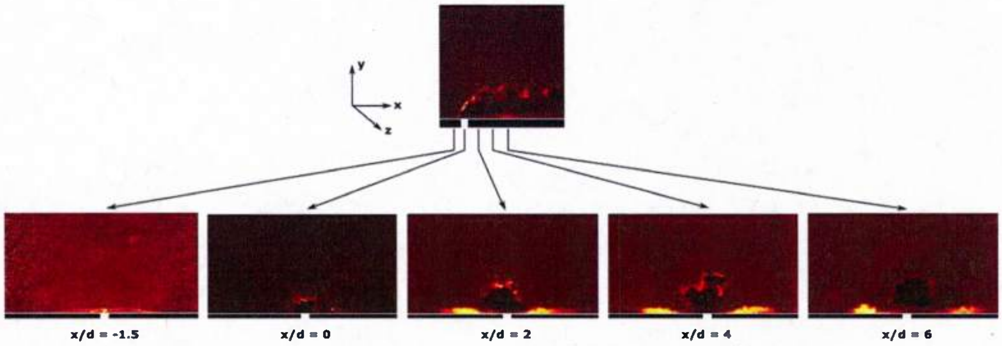

Figure 32. End views on several y-z planes (at different x/d locations) of sonic hydrogen jet injected into the supersonic crossflow (M = 2.7) at J = 2.4. Freestream conditions are T = 1500 K, T_o = 2800 K, p = 40 kPa.

shows a composite image of several plan-view planes at y/d = 0.25, 0.5, 1, 2, and 3. Finally, Fig. 32 shows the corresponding end-view planes at x/d = -1.5, 0, 2, 4 and 6. The PLIF imaging is tuned to the hydroxyl radical at the reaction zone; however, due to contamination of the freestream with fluorescing residues from the burst diaphragms, high levels of freestream noise are present. Although this noise in the freestream is unwanted, it unintentionally offers some insight on the injection of pure jet fluid (that appears as completely dark regions) and on the location of the bow shock forming on the front of the transverse jet.

Figure 33. Centerplane side-views (z/d = 0) of a sonic hydrogen jet injected into the supersonic crossflow (M = 2.4) at J = 2.4 and (a) 60° injection angle, and (b) 30° injection angle. Freestream conditions are T = 1500 K, T_o = 2800 K, p = 40 *kPa*.

This extensive imaging reveals the complex nature and structure of flame ignition and stabilization. Under these injection conditions three major features are seen from the results: a strong, intermittently reacting recirculation region on the frontal region of the jet, a reactive shear layer in the mixing region of the windward side of the transverse jet, and a highly reactive boundary layer – a feature of particular interest. As clearly shown in Figs. 29 and 30, the thin boundary layer ignites in the recirculation region in front of the transverse jet and wraps around the base of the bow shock cell that surrounds the jet. The reacting boundary layer propagates downstream, resembling the horseshoe vortex of incompressible jets in crossflow, and it propagates and is entrained in the wake of the transverse jet. The presence of ongoing reaction in the boundary layer also indicates strong entrainment of jet fluid into the recirculation region of the jet and into the boundary layer. Fuel entrainment in the reacting boundary layer might be a significant mechanism for flame stabilization and ignition in the far field of these transverse jets. Similar spatial features are seen as the jet-to-crossflow momentum ratio is increased; however, as the freestream temperature is lowered, the reacting boundary layer disappears, although fuel entrainment still is expected to be present. Furthermore, the near field stability of these reacting jets is lost as the injection angle decreases from 90° down to 60° (Figs. 33a and 34a) and completely disappears at injection angles of 30° (Figs. 33b and 34b).

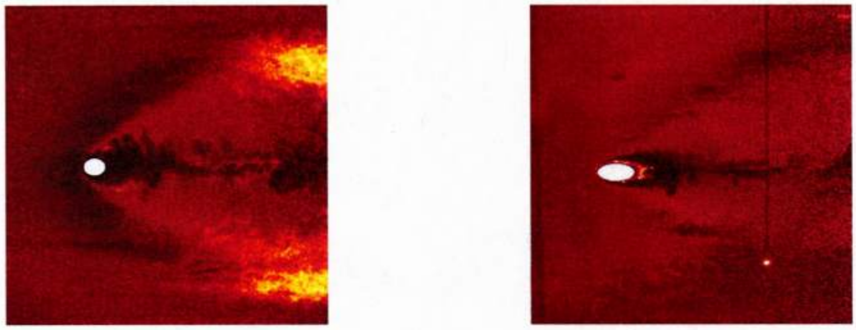

(a) (b)

Figure 34. Plan-views at y/d = 0.25 of sonic hydrogen jet injected into the supersonic crossflow (M = 2.4) at J = 2.4 and (a) 60° injection angle, and (b) 30° injection angle. Freestream conditions are T = 1500 K, T_o = 2800 K, p = 40 kPa.

3.5.4. Diode-Laser Diagnostics for Expansion Tube Characterization

The objective of this work was to develop a new diagnostic technique that would enable the characterization of the free-stream conditions of the Stanford 6-inch expansion tube facility. Two successive generations of tunable diode laser (TDL)-based H_2O absorption diagnostics were developed for the purpose of time-resolved characterization of the expansion tube free-stream conditions.

The first generation of the diagnostic was designed to measure static temperature using direct absorption thermometry applied with a pair of beam paths oriented perpendicular to the free-stream flow (Fig. 35a). Static temperature was successfully measured (Fig. 35b); however, the harsh conditions present in the expansion tube underscored several limitations of the direct absorption thermometry technique, including sensitivity to beam steering and background emission, as well as a limited signal-to-noise ratio.

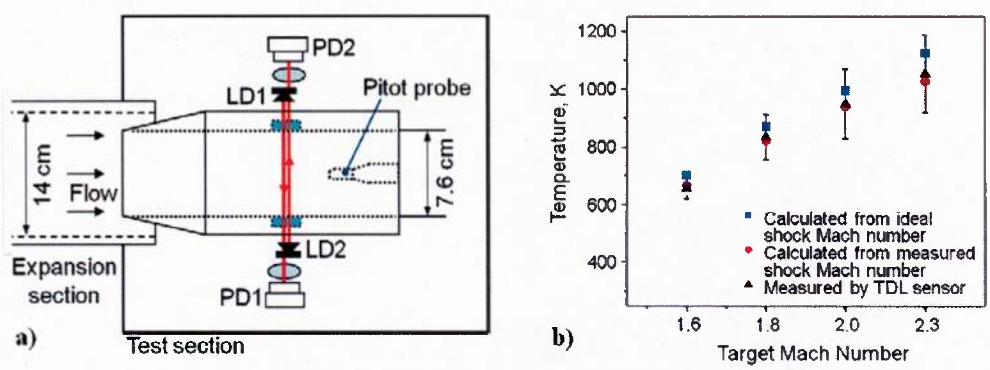

Figure 35. First generation TDL diagnostic. (a) Schematic of diagnostic. (b) Comparison of temperature measurements to isentropic predictions for several test conditions.

The second generation diagnostic leveraged the insight gained from the limitations of the previous diagnostic and was designed to measure both temperature and velocity simultaneously. This result was accomplished with a crossed beam configuration of two co-propagating lasers (Fig. 36a) and the incorporation of the technique of Doppler shift velocimetry. To mitigate the sensitivities and low signal-to-noise ratio of the previous diagnostic, the technique of wavelength modulation spectroscopy with second harmonic detection (WMS-2f) thermometry replaced the use of direct absorption thermometry. Both the temperature and velocity of the free-stream flow were measured (Fig. 36b) and provided insight into the thermodynamic and kinetic state of the free-stream over the duration of the test time. Unexplained scatter within the temperature and velocity data prompted identification of deficiencies within the WMS-2f theory. These deficiencies now are being addressed in the development of an extended WMS-2f theory.

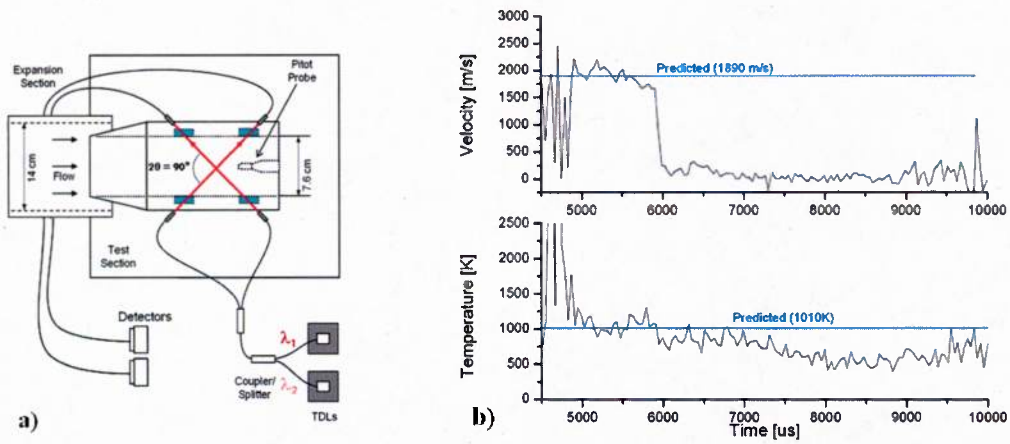

Figure 36. Second generation TDL diagnostic. (a) Schematic of diagnostic. (b) Illustrative temperature and velocity measurements and corresponding isentropic predictions.

3.6 Plasma-Assisted Subsonic and Supersonic Combustion (PIs: Cappelli, Mungal)

The main objective of this study was to develop an understanding of how non-equilibrium gas discharge plasmas enhance combustion under subsonic (premixed/partially premixed) and supersonic (partially premixed) flow conditions. The major achievements of this task are as follows:

1) Greatly extended the blow-off limit in partially-premixed methane jets in co-flow and cross-flow air configurations.
2) Extended the stability of premixed methane-air flames to well below the lean flammability limits.
3) Identified nonequilibrium plasma reforming of the fuel to produce intermediate molecular hydrogen and carbon monoxide as the key mechanism for flame stabilization in these subsonic flow conditions and verified this mechanism by studies at high temperature and by flame modeling.

4) Demonstrated the use of nonequilibrium plasmas in conjunction with wall cavities to enhance the combustion of hydrogen jets in a supersonic air/oxygen cross-flow.
5) Developed a novel two-jet strategy to eliminate the need for wall cavities in stabilizing supersonic combustion.

3.6.1. Plasma-enhanced combustion stabilization of methane jets in co-flow and cross-flow air

We have compared various non-equilibrium discharges for their propensity to extend the stability of methane jets in co-flow air. These discharges include so-called corona discharges, dielectric barrier discharges, as well as ultra-short repetitively pulsed (nanosecond) discharges – or USRD. The latter discharges (USRD) exhibit highly desirable properties, particularly the controlled termination of the pulsed electric field in time, to prevent Ohmic heating of the gas by electron-neutral collisions. With voltages of approximately 10 kV over discharge gaps of about 1 mm, the relatively high electric field strength (10^7 V/m) applied over a time of approximately 1 ns leads to very high average electron energy, channeling this energy primarily into bond breaking to form radicals. This strong thermal and chemical nonequilibrium results, as shown in Fig. 37, in greatly enhanced flame stability, with nanosecond pulsed discharges (shown in green) able to extend the blow-out limit by nearly a factor of ten on the co-flow speed and nearly 2.5 times on the jet speed with only several watts of discharge power, amounting to less than 0.1% of the chemical output power of the flame. This enhanced stability, particularly with the USRD, also was seen in cross-flow configurations – a more complex flow/jet interaction. Like the co-flow studies, stability is optimized for particular discharge placement (see Fig. 38). Our experiments determined that optimum stability (as established by the duty cycle in the flame flutter) is achieved when the discharge is placed in a region of the partially-premixed flame where the local equivalence ratio is approximately 0.63 times that of the stoichiometric value for methane/air mixtures. These works were published in three major papers (see publications list), and the details may be found in these papers.

3.6.2. Extended stability of premixed methane-air flames.

In atmospheric pressure premixed methane-air flames, nonequilibrium nanosecond discharges were found to extend the stability (blow-off limit) greatly beyond the lean flammability limit by some 15-20%, with minimal invested power (0.01% the chemical power of the flame - several watts). Spectroscopic investigations, as well as thermal and chemical probing of this flame, revealed that it is comprised of two distinct luminous zones, one just downstream of the nanosecond pulsed discharge, which is relatively cool (<600K), referred to as a pre-flame, and the other, the luminous hotter region associated with the combustion of the surrounding flow. The preflame now is understood to be a region of chemical reforming of methane to produce H_2 and CO. These intermediate species increase the surrounding flame stability.

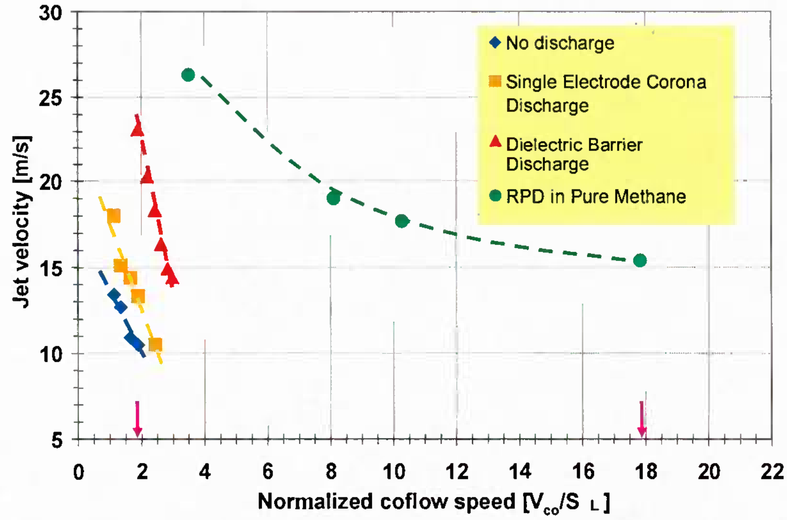

Figure 37. Jet (methane) velocity for flame blow-off versus co-flow air velocity (normalized to the stoichiometric laminar flame speed) for various nonequilibrium plasma sources.

3.6.3. Fuel reforming by nanosecond nonequilibrium discharge

Our research findings point to a relatively novel mechanism for premixed flame stabilization, which also extends to partially premixed conditions. We have deduced that the nonequilibrium discharges generate copious levels of reactive radicals in the near field (<mm) of the discharge, but in short time these radicals recombine and in the far field generate the relatively stable species (H_2 and CO, as mentioned earlier). This plasma-activated stream (in the near and far-field) constitutes the visible "preflame", combusting the fuel under lean and cold flow conditions. The combustion products of this inner preflame, including thermal energy and radicals, then serve as a pilot to ignite the bypass lean methane air stream, leading to the strongly visible "outer flame" amongst other features. We have proposed a model for this plasma-sustained combustion process (see Fig. 39, left frame) and have carried out simulations that predict the presence of a nested two-flame structure. Measurements of H_2 and CO, as well as NOx, are in reasonable quantitative agreement with model predictions.

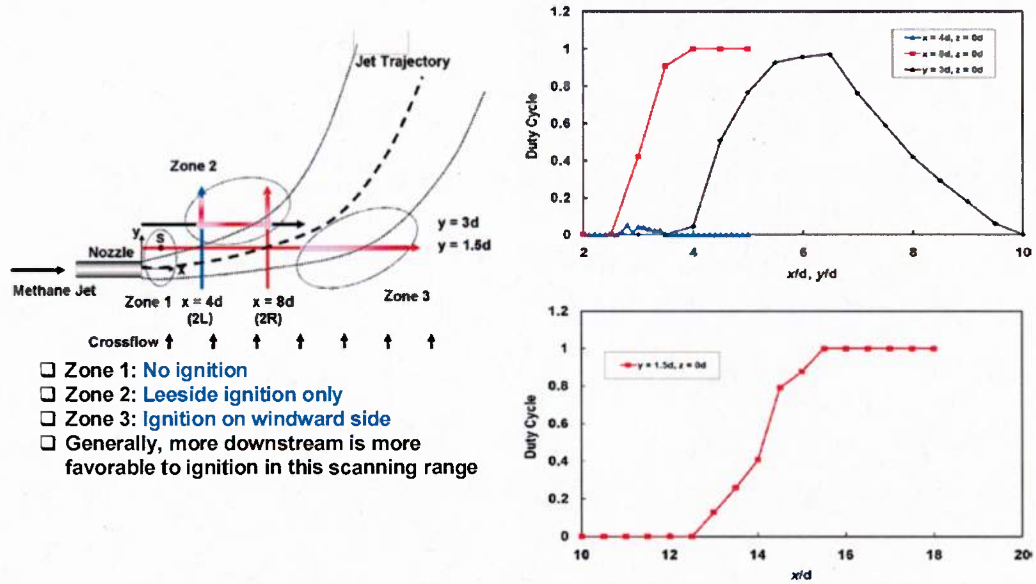

Figure 38. Jet (methane) flame in a cross flow configuration. (Left) schematic depicting zones of discharge placement and (right) variation in the measured duty cycle (stability). Stability favors leeside (zone 2) and windward side far from the jet nozzle (zone 3).

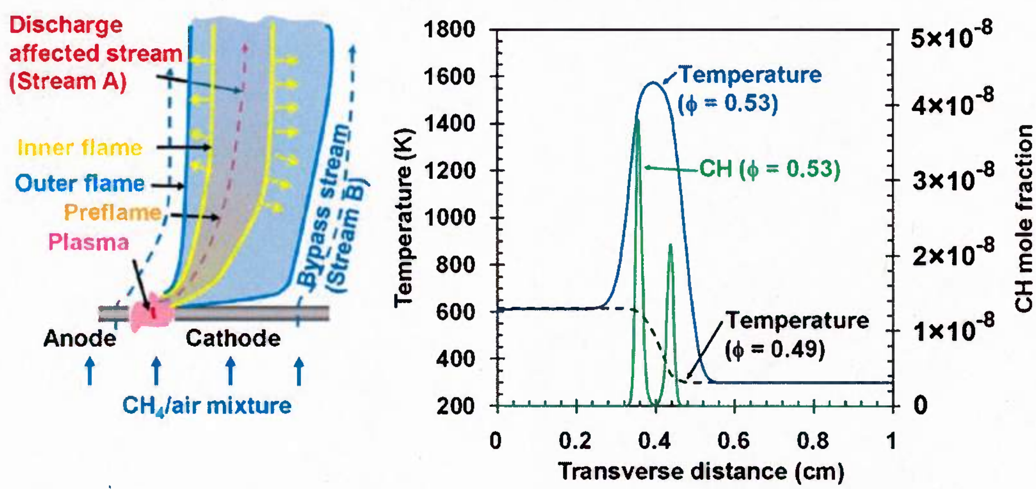

Figure 39. Model of premixed methane-air plasma-assisted combustion (left) and results of numerical simulations depicting the ensuing two-flame structure (right).

3.6.4. Plasma-augmentation of wall cavity-assisted supersonic combustion.

We have employed nanosecond pulsed plasma discharges located within a wall cavity to ignite jet flames (hydrogen and ethylene) in supersonic crossflows. The nonequilibrium plasma is produced by repetitive pulses of 15 kV peak voltage, 20 ns pulse width, and 50 kHz repetition rate. Sonic fuel jets are injected into free stream air of Mach numbers M = 1.7 to M = 3.0. Combustion is found to be enhanced by the plasma discharge (see Fig. 40), in part due to a reduction in ignition delay time (by as much as 40 μs). Similar trends are observed with both hydrogen and ethylene fuel injection. The experimental results for

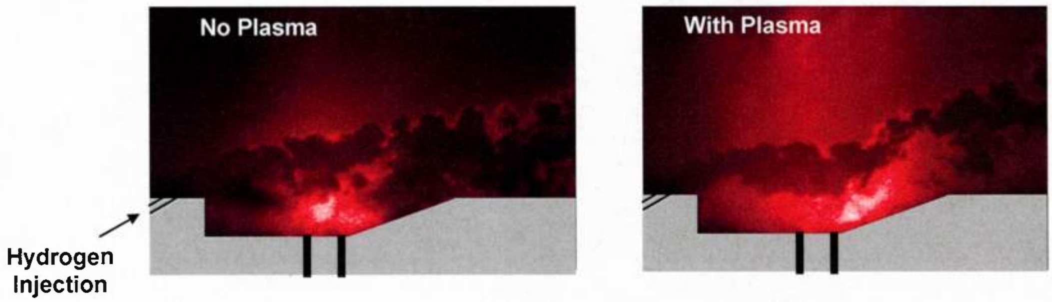

Figure 40. Enhanced combustion of hydrogen injected into supersonic air using nanosecond pulsed discharge inside a wall cavity. Left: no discharge. Right: with discharge plasma.

hydrogen combustion are interpreted using a simple model in which the pulsed plasma serves as a repetitive source of reactive radicals. The model description allows us to predict how a broader range of plasma operation conditions will affect combustion.

3.6.5. Plasma-assisted supersonic combustion without wall cavities.

In the absence of a wall cavity flame ignition and stability are difficult to achieve under the conditions in Fig. 40. For combustion in the absence of a wall cavity, we have used a nanosecond pulsed plasma discharge located between two fuel jets to ignite jet flames (hydrogen and ethylene) in supersonic crossflow (see Fig. 41). The fuel injection nozzles and discharge electrodes are mounted flush with the surface of a flat wall, and the nonequilibrium plasma is produced by repetitive pulses of 15 kV peak voltage, 20 ns pulse width and 50 kHz repetition rate. Fuel jets are injected into free stream oxygen of Mach numbers M = 1.7 - 3.0. A configuration combining an upstream subsonic oblique jet and a downstream sonic

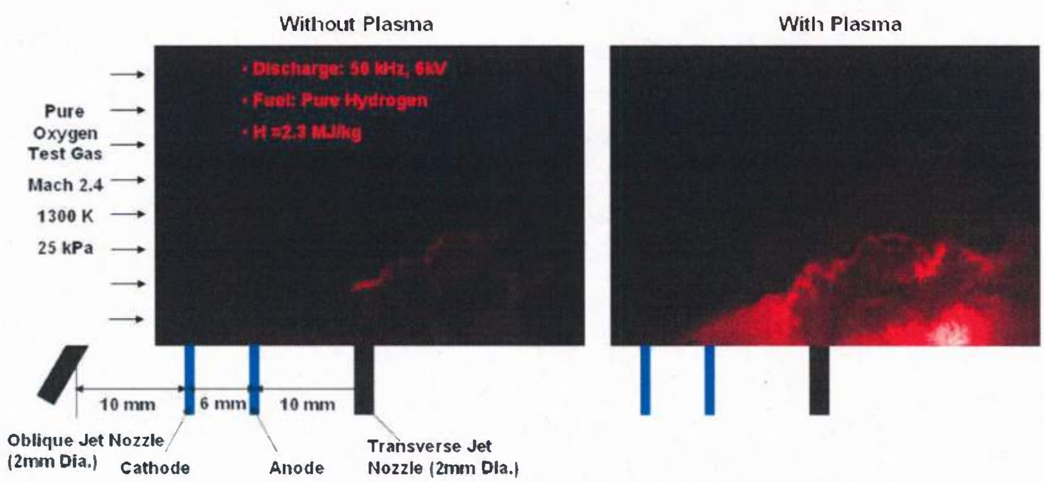

Figure 41. Enhanced combustion of hydrogen injected into supersonic air using nanosecond pulsed discharge in a dual jet configuration. Left: no discharge. Right: with discharge plasma.

transverse jet is shown to provide adequate flow conditions for jet flame ignition assisted by the plasma discharge. The upstream jet bleeds fuel into the boundary layer, which then is dissociated by the discharge and ignited. This flame then serves to pilot the combustion of the main downstream jet. The experimental results are interpreted using a simple model in which the pulsed plasma serves as a source of reactive radicals added to a flammable gas mixture.

3.7 Large-Eddy Simulation of Jet Mixing in a Supersonic Crossflow (PI: Lele)

The main objective of this study is to get further insight into the three-dimensional complex flow physics of the jet mixing in supersonic crossflows using large-eddy simulation (LES). The major accomplishments of this topic are summarized as follows:

1) Improvement of numerical scheme for the interaction of turbulence with shocks and material discontinuities
2) The successful simulation of a supersonic turbulent boundary layer (for providing realistic turbulent inflow)
3) The successful simulation of jet mixing in supersonic crossflows (JISC) with a laminar/turbulent boundary layer

3.7.1. Numerical scheme for interaction of turbulence with shocks and material discontinuities

We developed the localized artificial diffusivity (LAD) scheme to simulate the physics of JISC accurately where the high-speed flows contain complex, dynamic shock-turbulence interactions. The numerical scheme and high-order compact scheme with LAD, can capture different types of discontinuities (shocks, contact/material surfaces) and also resolve the broadband scales of turbulence with better accuracy and less computational cost than well-known high-order shock-capturing schemes (e.g. WENO schemes [17], see Fig. 42). Investigations of the impact of the subgrid model and other implicit dissipative processes on flow phenomena also were assessed carefully within the framework of the numerical scheme developed. These works were published in three major papers in the *Journal of Computational Physics* (see list in Sec. 5), and the details may be found in these papers.

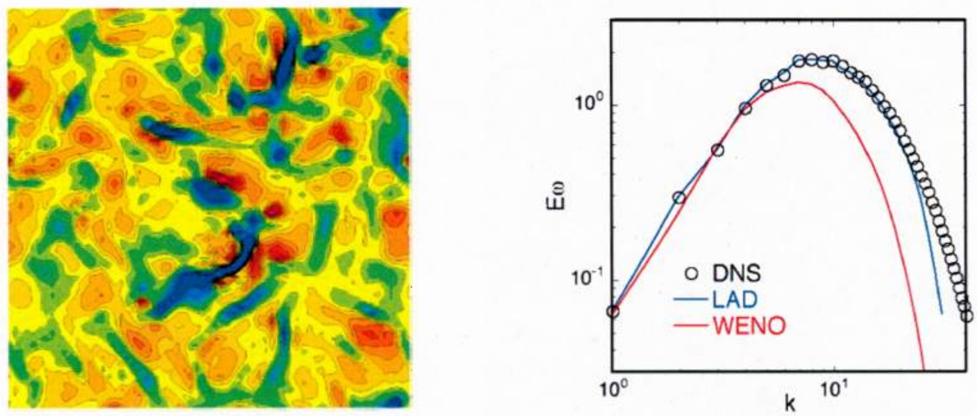

(a) (b)

Figure 42. Compressible decaying isotropic turbulence with shocklets: (a) dilatation contours and (b) vorticity spectra (k is the wavenumber and E_ω is the power spectral density).

3.7.2. Supersonic turbulent boundary layer

LES of supersonic turbulent boundary layers was performed by using the LAD scheme. A compressible extension of rescaling-recycling method is used for the inlet boundary [18]. Three levels of mesh refinement were conducted. A fully developed turbulent boundary layer profile with a logarithmic region was captured properly. The statistics of time-averaged and fluctuation quantities well agreed with existing DNS data (Fig. 43). The result shows the capability of our numerical scheme to simulate the supersonic wall-bounded turbulence within the framework of LES. This LES of supersonic turbulent boundary layers was coupled with LES of JISC for the inflow conditions of JISC with turbulent crossflow to investigate the effects of crossflow turbulence on mixing.

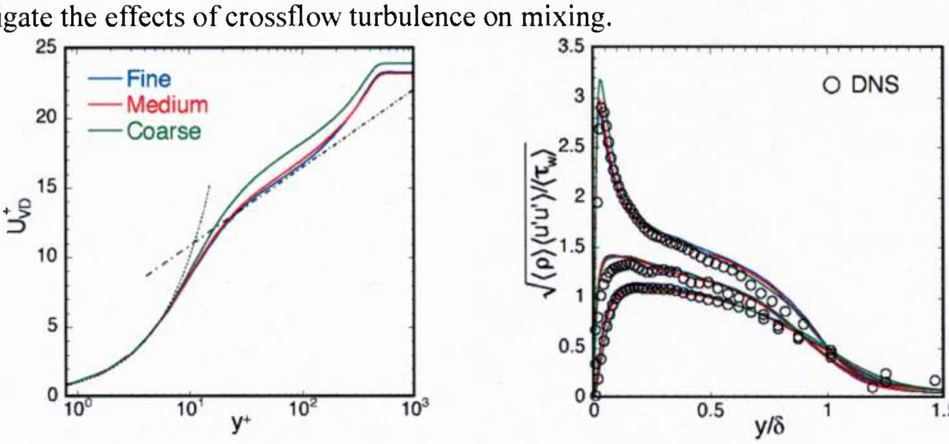

(a) (b)

Figure 43. Mean and fluctuating velocity profiles in a M=1.6 supersonic turbulent boundary layer. (a) mean velocity and (b) velocity fluctuations.

3.7.3. Jet mixing in supersonic turbulent/laminar crossflows

LES of a sonic jet injection into supersonic crossflows was conducted to obtain insight into the key physics of jet mixing. A high-order compact differencing scheme with the LAD scheme for discontinuity capturing is used. The flow conditions are the same as in the experiments of Ref. 19, with $M_{crossflow}$=1.6, Re_D=2.4x10^4 and jet-to-crossflow momentum flux ratio J=1.7. Detailed comparisons with these experimental data were conducted. Jet mixing calculations where the upstream boundary layer is fully turbulent (Fig. 44) were compared with corresponding calculations with a nominally laminar boundary layer to elucidate the effect of the approaching turbulent boundary layer on the jet mixing mechanisms.

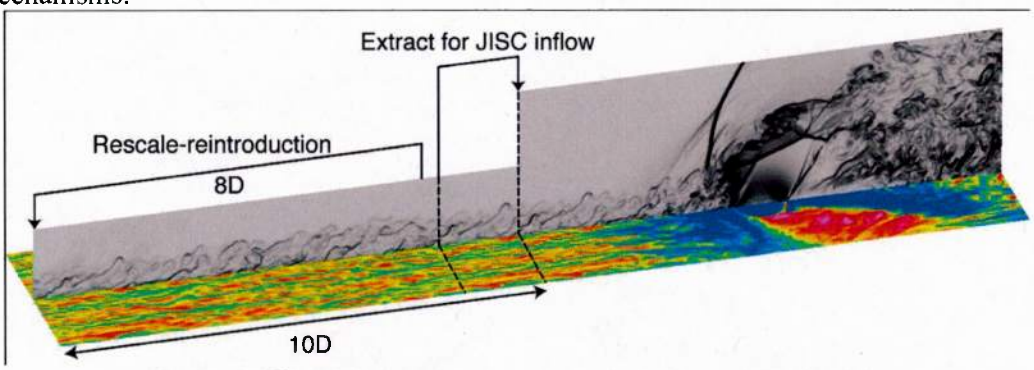

Figure 44. JISC with incoming supersonic turbulent boundary layer.

Statistics obtained by the LES for turbulent crossflow showed good agreement with the available experiments. Note the dramatic improvement in the predicted mean velocity profiles at the jet upstream x/D=-1.5 station for the turbulent crossflow calculation (Fig. 45). A progressive mesh refinement study was conducted to quantify the broadband range of scales of turbulence that are resolved in the simulations. The three levels of mesh refinement showed reasonable grid convergence in the predicted mean and turbulent flow quantities (e.g., Fig. 45). Thus LES is deemed suitable for exploration of the physics and dynamics of the jet mixing in a supersonic turbulent crossflow.

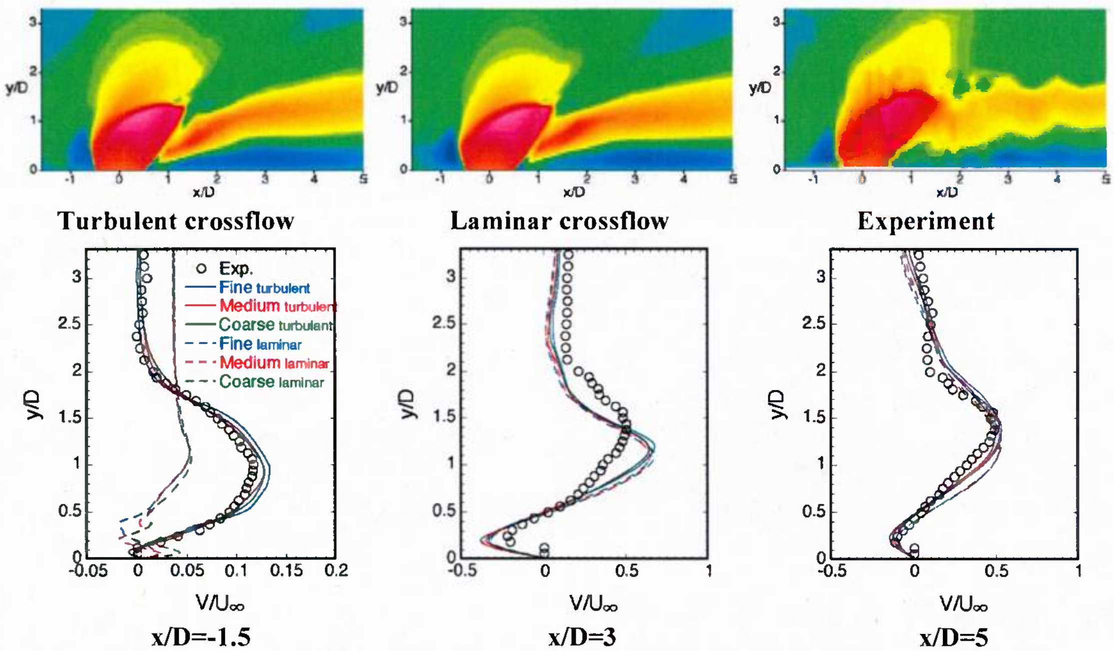

Figure 45. Comparisons of mean wall-normal velocity between LES with turbulent and laminar crossflows on three levels of mesh resolution and experimental data.

With regard to the processes controlling the jet mixing, we studied the key physics of the jet mixing in supersonic crossflows. Relatively large-scale clockwise and counter-clockwise rotating longitudinal vortices form two pairs of counter-rotating vortices (A and B in Fig. 46). Relatively small-scale hairpin-like vortices are generated along the longitudinal vortices. The relatively large-scale longitudinal vortex structures break down into finer and random turbulent structures downstream of the hairpin vortices. The jet surfaces are elongated along the relatively large-scale longitudinal vortex structures (C in Fig. 46) and break down to finer and more random structures in the developed turbulent region, indicating the importance of these eddy structures that determine the behavior of jet fluid stirring and subsequent mixing.

The simulated unsteady flowfield shows noticeable repeated large-scale dynamics of the deformation of shock structures and accompanying vortex formation. Pressure fluctuations inside the recirculation region are coupled with the large-scale unsteady dynamics of the barrel shock and the bow shock deformation and accompanied large-scale vortex formation in the windward jet boundary. During the repeated large-scale dynamics, the rolled-up windward jet shear layer is entrained into an upstream separation

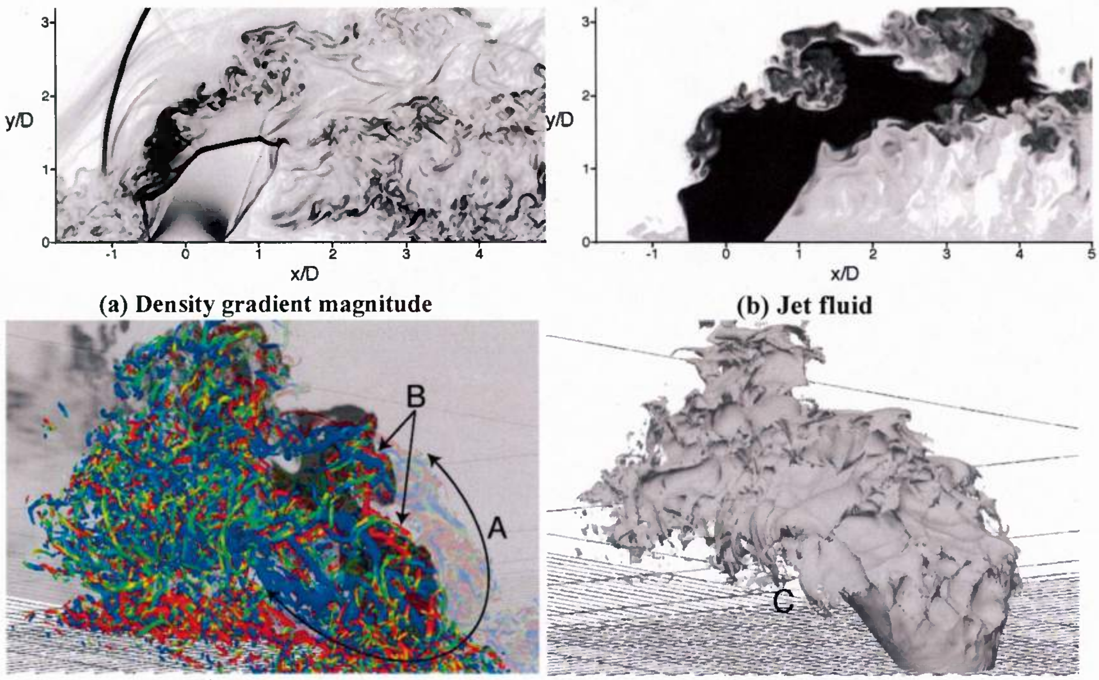

(a) Density gradient magnitude (b) Jet fluid

(c) Vortex structures (d) Jet structures

Figure 46. Instantaneous snapshots of key vortex and jet structures

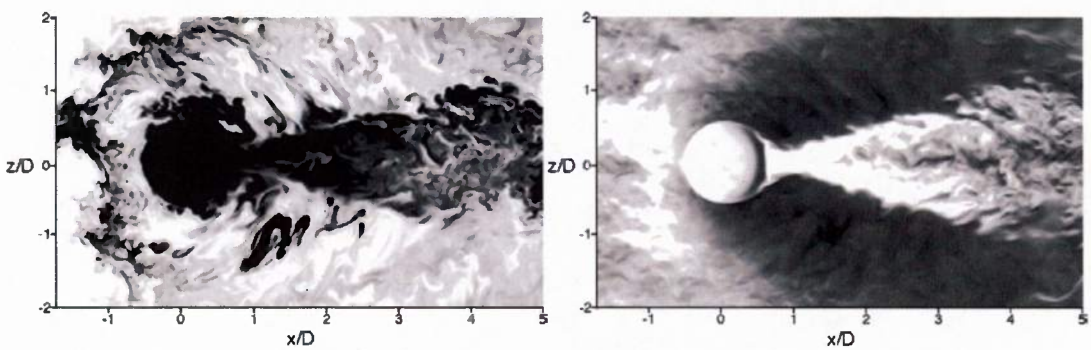

Figure 47. Representative instantaneous snapshots of jet fluid (left) and streamwise velocity (right) at wall-parallel plane close to the wall.

region, showing the intermittent upstream jet fluid mixing (Fig. 47). The simulated flowfield also shows the continuous jet fluid entrainment into the boundary layer separation bubble downstream of the jet injection.

Comparisons between the turbulent and laminar crossflows illustrate the importance of turbulent structures in the upstream boundary layer on the jet mixing mechanism. The interaction between the turbulent structures in the upstream incoming boundary layer and the jet enhances the instability of the windward jet shear layer, which supports a more rapid breakdown in the jet shear layer structure to the turbulent state. Thus, with the turbulent crossflow the jet fluid is stirred progressively with the crossflow, entrained into the flow, and subsequently mixing is enhanced.

4. REFERENCES

1. Curran, E. T., Heiser, W. H. and Pratt, D. T. (1996), "Fluid Phenomena in Scramjet Combustion Systems," Annual Review of Fluid Mechanics, Vol. 28, pp. 323-360, 1996.
2. Clemens, N.T. and Narayanaswamy, V., "Shock/Turbulent Boundary Layer Interactions: Review of Recent Work on Sources of Unsteadiness," AIAA paper 2009-3710, June 2009.
3. Hutchins, N., Marusic, I., "Evidence of very long meandering structures in the logarithmic region of turbulent boundary layers," *Journal of Fluid Mechanics*, Vol. 579, pp. 1-28, 2007.
4. Lin, J. C., "Review of Research on Low-Profile Vortex Generators to Control Boundary-Layer Separation," *Progress in Aerospace Sciences*, Vol. 38, No.4, pp. 389-420, 2002.
5. Pearcey, H. H., Rao, K., Sykes, D. M. (1993), "Inclined Air-Jets Used as Vortex Generators to Suppress Shock-Induced Separation," AGARD-CP-534, *Computational and Experimental Assessment of Jets in Cross Flow*, pp. 40.1-40.10, Winchester, UK, 19-22 April, 1993.
6. Milanovic, I. M., Zaman, K. B. M. Q., "Fluid Dynamics of Highly Pitched and Yawed Jets in Crossflow," *AIAA Journal*, Vol. 42, No.5, May 2004, pp. 874-882, 2004.
7. Akella, M.R., "Immersion and Invariance Based Adaptive Control for Nonlinear Multi-Input Multi-Output Systems," Proceedings of the SES Annual Meeting, October 2007.
8. Akella, M.R., and Subbarao, K., "A Novel Parameter Projection Mechanism for Smooth and Stable Adaptive Control," *Systems and Control Letters*, Vol. 54, No. 1, pp. 43-51, January 2005.
9. Daren, Y., Tao, C. and Wen, B., "Equilibrium Manifold Linearization Model for normal Shock Position Control Systems," *Journal of Aircraft*, Vol. 42, No. 5, pp. 1344–1347, 2005.
10. Chunodkar, A., and Akella, M.R., "Attitude Stabilization with Network Delay in Feedback Control Implementation," AIAA Guidance, Navigation, and Control Conference, Chicago, IL, August, Paper Number AIAA-2009-5801, 2009.
11. Chunodkar, A., and Akella, M.R., "Robust Attitude Stabilization in Presence of Unknown Time-Varying Time-Delays ," 2010 AAS/AIAA Space Flight Mechanics Meeting, San Diego, CA, February, Paper Number AAS-10-274, 2010.
12. MacMartin, D., "Dynamics and Control of Shock Motion in a Near-Isentropic Inlet," Journal of Aircraft, Vol. 41, No. 4, pp. 846–853, 2004.

13. Tao, C., Daren, Y., Wen, B. and Yongbin, Y., "Gain Scheduling Control of Nonlinear Shock Motion Based on Equilibrium Manifold Linearization Model," Chinese Journal of Aeronautics, vol. 20, pp. 481–487, 2007.

14. Lisovskiy, V.A. and Yakovin, S.D., "Experimental study of a low-pressure glow discharge in air in large-diameter discharge tubes: I. conditions for the normal regime of a glow discharge," Plasma Physics Reports, Vol. 26, pp. 1066-1075, 2000.

15. Trimpi, R.L., "A preliminary theoretical study of the expansion tube, a new device for producing high-enthalpy short-duration hypersonic gas flows", NASA TR R-133, 1962.

16. Anderson, G.Y. and McClinton, C.R. and Weidner, J.P., "Scramjet performance", in Scramjet Propulsion, E.T. Curran and S.N.B. Murthy Eds., 2000.

17. Weirs, G. and Candler, G., "Optimization of Weighted ENO Schemes for DNS of Compressible Turbulence," AIAA Paper No. 97-1940, 1997.

18. Kawai, S., Shankar, S. K. and Lele, S. K., "Assessment of localized artificial diffusivity scheme for large-eddy simulation of compressible turbulent flows," *Journal of Computational Physics*, vol. 229, issue 5, pp. 1739-1762, 2010.

19. Santiago, J.G. and J.C. Dutton, "Velocity Measurements of a Jet Injected into a Supersonic Crossflow," *Journal of Propulsion and Power*, 13, 2, pp. 264-273, 1997.

5. ARCHIVAL PUBLICATIONS RESULTING FROM THIS GRANT

1. T. Deconinck, S. Mahadevan and L. L. Raja, "Simulation of Direct-Current Surface Plasma Discharge Phenomena in High-Speed Flow Actuation," IEEE Transactions on Plasma Science, Vol. 35, No. 5, Oct 2007, pp. 1301-1311.

2. T. Deconinck, S. Mahadevan and L. L. Raja, "Discretization of the Joule Heating Term for Plasma Discharge Fluid Models in Unstructured Meshes," *Journal of Computational Physics*, Vol. 228, No. 12, pp. 4435-4443, 2009.

3. S. Mahadevan and L. L. Raja, "Simulations of direct-current air glow discharge at pressures ~ 1 Torr: discharge model validation," *Journal of Applied Physics*, (in print), 2010.

4. S. Mahadevan and L. L. Raja, "High-fidelity computational model of direct-current surface plasma actuator for high-speed flow control," AIAA Journal, submitted 2010.

5. Ganapathisubramani, Lakshminarasimhan, K. and Clemens, N.T., "Investigation of three-dimensional structure of fine scales in a turbulent jet by using cinematographic stereoscopic particle image velocimetry", Journal of Fluid Mechanics, Vol. 598, pp. 141-175, 2008

6. J. Shin, Clemens, N.T., and Raja, L.L., "Schlieren Imaging of Flow Actuation Produced by Direct-Current Surface Glow Discharge in Supersonic Flows," IEEE Transactions on Plasma Science, Vol. 36, No. 4, August 2008

7. Ganapathisubramani, Clemens, N.T. and Dolling, D.S., "Low-frequency dynamics of shock-wave/boundary-layer interactions," *Journal of Fluid Mechanics*, Vol. 636, pp. 397-425, 2009.

8. V. Narayanaswamy, Raja, L.L. and Clemens, N.T., "Characterization of a high-frequency pulsed plasma jet actuator," *AIAA Journal*, Vol. 48, No. 2, pp. 297-305, February 2010.

9. J. Wagner, K.B. Yuceil, A. Valdivia, N. Clemens, and D. Dolling, "An experimental investigation of unstart in an inlet/isolator," *AIAA Journal*, Vol. 47, No. 6, pp. 1528-1542, 2009.

10. J. Wagner, K.B. Yuceil, N. Clemens, "PIV Measurements of Unstart of an Inlet/Isolator Model in a Mach 5 Flow," *AIAA Journal*, to be published, 2010.

11. S. Kawai and S. K. Lele, "Localized artificial diffusivity scheme for discontinuity capturing on curvilinear meshes," Journal of Computational Physics, vol. 227, issue 22, pp. 9498-9526, 2008

12. B. Fiorina and S. K. Lele, "An artificial nonlinear diffusivity method for supersonic reacting flows with shocks," Journal of Computational Physics, vol. 222, issue 1, pp. 246-264, 2007.

13. S. Kawai and S. K. Lele, "Large-eddy simulation of jet mixing in supersonic crossflows," AIAA Journal, revision submitted, 2010.

14. S. Kawai, S. K. Shankar and S. K. Lele, "Assessment of localized artificial diffusivity scheme for large-eddy simulation of compressible turbulent flows," *Journal of Computational Physics*, vol. 229, issue 5, pp. 1739-1762, 2010.

15. W. Kim, H. Do, M.G. Mungal, and M.A. Cappelli, "Plasma-discharge stabilization of jet diffusion flames," IEEE Transactions on Plasma Science 6, pp. 2545-2551, 2006.

16. W. Kim, H. Do, M. G. Mungal and M. A. Cappelli, "Investigation of NO production and flame structure in plasma enhanced premixed combustion," Proceedings of the Combustion Institute, 31(2), pp. 3319-3326, 2007.

17. W. Kim, H. Do, M. G. Mungal & M. A. Cappelli (2007) "On the role of oxygen in dielectric barrier discharge actuation of aerodynamic flows," Applied Physics Letters, 19, 181501

18. W. Kim, M. G. Mungal & M. A. Cappelli (2008) "Formation and role of cool flames in plasma assisted premixed combustion," Applied Physics Letters, 92, 051503

19. H. Do, W. Kim, M. A. Cappelli and M. G. Mungal (2008) "Cross-Talk in Multiple Dielectric Barrier Discharge Actuators," Applied Physics Letters, 92, 071504

20. W. Kim, H. Do, M. G. Mungal & M. A. Cappelli (2008) "Optimal discharge placement in plasma assisted combustion of a methane jet in crossflow," Comb. Flame, 153, 603–615

21. W. Kim, H.Do, M. G. Mungal, and M. A. Cappelli, "A Study of Plasma-Stabilized Diffusion Flames at Elevated Ambient Temperatures," IEEE Transactions on Plasma Science, 36, p. 2898-2904, 2008.
22. H. Do, M. G. Mungal and M. A. Cappelli (2008) "Jet Flame Ignition in a Supersonic Crossflow using a Pulsed Nonequilibrium Plasma Discharge," to appear IEEE Transactions on Plasma Science.
23. W. Kim, M. G. Mungal and M. A. Cappelli, "The role of in-situ reforming in plasma enhanced ultra lean premixed methane/air flames," Combustion and Flame, 157, pp. 374-383, 2010.
24. H. Do, M. A. Cappelli, and M. G. Mungal, "Plasma assisted cavity flame ignition in supersonic flows," Combustion and Flame, submitted, September, 2009.
25. H. Do, S.K. Im, M. A. Cappelli, and M. G. Mungal, Plasma assisted flame ignition in supersonic flows using dual jet injection, *Combustion and Flame*, submitted, February, 2010.
26. S. Srikant, and M.R. Akella, "Persistence Filter Based Control for Systems with Time-Varying Control Gains," Systems and Control Letters, Vol. 58, No. 6, June 2009.
27. Srikant, S., Valdivia, A., Wagner, J., Akella, M.R. and Clemens, N., "Unstart Detection in a Simplified Hypersonic Inlet-Isolator," Journal of Propulsion and Power, to be published, 2010.
28. J. Hatlelid, and M.R. Akella, "Robust Nonlinear Adaptive Tracking Control for Control Non-Affine Dynamical Systems," *AIAA Journal of Guidance, Control, and Dynamics,* submitted, 2010.

6. PH.D. DISSERTATIONS RESULTING FROM THIS GRANT

All Ph.D. dissertations are available through ProQuest UMI Microfilm (www.proquest.com).

1. Wookyung Kim, "An investigation of plasma enhanced combustion," Ph.D. Dissertation, Stanford University, June 2006.
2. T. Deconinck, "Simulation studies of direct-current microdischarges for electric propulsion," Ph.D. Dissertation, The University of Texas at Austin, December 2008.
3. Hyungrok Do, "Plasma-assisted combustion in a supersonic flow," Ph.D. Dissertation, Stanford University, May 2009.
4. W. N. Heltsley, "Structure and Stability of Reacting Jets in Supersonic Crossflow," Ph.D. Dissertation, Stanford University, June 2010.
5. J. L. Wagner, "Experimental Studies of Unstart Dynamics in Inlet / Isolator Configurations in a Mach 5 Flow," Ph.D. Dissertation, The University of Texas at Austin, May 2009.

6. V. Narayanaswamy, "Investigation of a pulsed plasma jet for separation shock control," Ph.D. Dissertation, The University of Texas at Austin, May 2010.
7. S. Mahadevan, "Simulation of supersonic flow phenomena in the presence of direct-current surface plasma actuators," Ph.D. Dissertation, The University of Texas at Austin, May 2010.
8. J. Shin, "A study of direct-current surface discharge plasma for a Mach 3 supersonic flow control," Ph.D. Dissertation, The University of Texas at Austin, December 2007.